

DESIGN, FABRICATION, AND DELIVERY OF A CHARGE INJECTION DEVICE AS A STELLAR TRACKING DEVICE

Final Technical Report
(November 28, 1977 to November 28, 1978)

H.K. Burke, G.J. Michon, H.W. Tomlinson, T.L. Vogelsong,
A. Grafinger, and R. Wilson

April 1979	(NASA-CR-161226) DESIGN, FABRICATION, AND DELIVERY OF A CHARGE INJECTION DEVICE AS A STELLAR TRACKING DEVICE Final Technical Report, 28 Nov. 1977 - 28 Nov. 1978 (General Electric Co.) 68 p HC A04/MF A01 . CSCL 03A 63/89	N79-24919 Unclas 20893

General Electric Company
Corporate Research and Development
Signal Electronics Laboratory
Schenectady, New York 12305
and
Aerospace Business Group
Re-Entry and Environmental Systems Research
and Engineering Department
Philadelphia, Pennsylvania 19101



George C. Marshall Space Flight Center
Huntsville, Alabama 35812



TABLE OF CONTENTS

<u>Section</u>		<u>Page</u>
1	1.0 INTRODUCTION	1
2	2.0 PROGRAM HISTORY	3
3	3.0 SYSTEM DESCRIPTION: CID ARRAY DESIGN	5
	3.0.1 Cell Layout	5
	3.0.2 Array Layout	5
	3.0.3 Array Parameters	6
	3.1 Readout Method	7
	3.2 Circuit Description	8
	3.2.1 Preamplifier Circuit	9
	3.2.2 Post Amplifier	10
	3.3 Timing Waveform Generation	10
	3.4 Data Collection and Processing	14
	3.5 Test Fixture Description	15
4	4.0 NOISE PERFORMANCE	17
	4.1 Theoretical Temporal Noise Levels	17
	4.1.1 Low Frequency Operation	20
	4.2 Fixed Pattern Noise	21
	4.3 Measured Results	21
5	5.0 SPECTRAL RESPONSE/QUANTUM YIELD	25
	5.1 Measured Results	25
	5.2 Temperature Effects	26
6	6.0 PROJECTED PERFORMANCE OF LARGE ARRAY	29
	6.1 Noise	29
7	7.0 SYSTEM STUDY RESULTS	33
	7.1 Requirements Summary	33
	7.2 Noise Models	36
	7.3 Acquisition Mode	37
	7.3.1 Effect of Image Velocity	37
	7.3.2 Effect of Position Error	38
	7.3.3 Frame Time	38
	7.4 Track Mode	40
	7.4.1 Accuracy/Stability	40
	7.4.2 Signal Integration Times	42
	7.4.3 Implementation Approaches	44
	7.5 Astrometry Mode	44
	7.5.1 Variable Magnitude	45
	7.5.2 Separation of Stars	45
	7.5.3 Magnitude Accuracy	45
	7.5.4 Complete Array Dump	45
	7.5.5 Implementation	45
	7.6 Computer Implications	46

TABLE OF CONTENTS (Cont'd)

<u>Section</u>		<u>Page</u>
8	8.0 CONCLUSIONS AND RECOMMENDATIONS	49
9	9.0 REFERENCES	51
10	10.0 APPENDIX	53
	10.1 Calculation of Tracking Accuracy and Stability	53
	10.1.1 Centered Star	55
	10.1.2 Star in Corner	58
	10.1.3 Case A	59
	10.1.4 Case B	60
	10.1.5 Case C	61

LIST OF ILLUSTRATIONS

<u>Figure</u>		
3-1	Cell Layout	5
3-2	Sensor Layout	6
3-3	Array Photomicrograph	7
3-4	Track Mode Background Rejection Technique	8
3-5	System Block Diagram	9
3-6	Preamplifier Schematic	10
3-7	Post Amplifier/DC Restore/Sample	11
3-8	Microcomputer Block Diagram	12
3-9	Overall Timing Diagram	12
3-10	Timing Diagram - Injection Sequence	13
3-11	Timing Diagram - Read Sequence	13
3-12	Typical Noise Data Printout	15
3-13	Test System Photograph	16
4-1	Measured Noise-Wafer #7	23
4-2	Measured Noise-Wafer #12	24
5-1	Signal Flow Diagram	25
5-2	Quantum Yield vs Wavelength: Wafer #7	26
5-3	Quantum Yield vs Wavelength: Wafer #12	27
7-1	Baseline Requirements	36
7-2	Radius of Stability vs Star Magnitude	41
7-3	Integration Time vs Visual Magnitude	43

LIST OF ILLUSTRATIONS (Cont'd)

<u>Figure</u>		<u>Page</u>
A-1	3 x 3 Pixel Sub-array	53
A-2	Light Distribution - Star in Center	54
A-3	Light Distrubution - Star in Corner	55

LIST OF TABLES

<u>Table</u>		
3-1	Electrical Parameters	7
4-1	Theoretical Noise Level	20
6-1	Theoretic Noise/Channel for 400 x 400 Array for Different Design Conditions	30
7-1	CID Base Line Design	33
7-2	Summary Comparison of Representative Star Tracker Requirements	34
7-3	Representative Worst Case Requirements	35
7-4	Noise Summary	36
7-5	Table of the Error Function	57

Section 1

1.0 INTRODUCTION

This program had two objectives: 1) to demonstrate the level of temporal and fixed pattern noise and the spectral quantum efficiency attainable with a Charge Injection Device (CID) imager operating a star tracking mode; and 2) to project the results to a conceptual 400 x 400 CID array for NASA star tracker applications.

Howard of General Electric⁽¹⁾ and Stanton et al. of the Jet Propulsion Laboratory⁽²⁾ have evaluated the potential tracking performance of a large CID sensor. The General Electric study used computer simulation and measured small CID characteristics to predict accuracy and data rate performance. Both studies concluded that the CID should be capable of meeting the application requirements with a minimum of associated equipment.

The outstanding features of the CID are high quantum efficiency, non-destructive readout, and simple interfacing with digital control electronics. The X-Y addressability of the CID sensor allows direct access to that portion of the array containing the image information. This feature allows operation at very low data rates and consequently allows low amplifier noise bandwidth. An operator can utilize the NDRO feature to perform repeated readouts of the image information or on-chip coding of the pixel quantities, both of which can lead to signal enhancement.

In this program a small (128 x 128) CID array, processed on bulk silicon and incorporating transparent upper-level conductors, was evaluated in a cooled breadboard camera. All the timing of waveforms and the processing of video data was done with a micro-computer. At the same time a system requirements study was performed to define performance goals and other operational requirements. Based upon performance of the large sensor as extrapolated from the test results, a tentative star tracker system was defined.

Section 2

2.0 PROGRAM HISTORY

During the course of this program it became necessary to slightly alter the initially proposed technical approach, particularly with regard to array fabrication, packaging, and readout methods.

The proposal to include preamplifier transistors within the array package proved burdensome in this experimental test system and was abandoned for devices mounted outboard of the array package. While this choice required greater scrutiny of electrical interference and increased measured output noise (to an unknown degree), it facilitated packaging, handling, and testing of devices. More importantly, it permitted direct comparison of the imager noise characteristics, unaffected by preamplifier parameter variations.

The initial readout concept, in which a relatively long time interval occurred between the resetting of the output bus and the single signal sample, placed a stringent requirement on device junction leakage current, which in turn added shot noise to the readout signal. When researchers encountered more junction leakage than expected on the earlier processed arrays, they devised new readout approaches to minimize this effect. Section 3 details a new approach in which the array is read out at a higher rate, non-destructively, and successive digital summations are taken to obtain an average signal. Because the processing gain obtained by summation balances the excess thermal noise incurred by the increase in bandwidth, system thermal (Johnson) noise remains unaffected, while the effect of junction leakage is greatly reduced by repeated reset operations at the readout rate. Another benefit of this operation mode is that problems associated with low frequency amplification, drift, $1/f$ noise, etc., are equivalently reduced. Subsequently, researchers determined and corrected the causes of the high rate of junction leakage; however, the summation- and-averaging readout approach was retained for its operational ease and other peripheral benefits.

The third and last change was the substitution of thin ($\approx 500\text{\AA}$) polysilicon for metal-oxide as an upper level conductor. Although it was introduced as a "back-up" approach when processing problems with the metal oxide were encountered, the polysilicon proved superior to the metal oxide in several significant ways. These include ease of fabrication, compatibility with present semiconductor processing, and superior spectral performance (an unaccounted for result at this writing). The higher resistance of the thin conductors is not a performance factor in the subject application because of the low readout rates and the fact that readout occurs on the orthogonal (high conductivity) lines. To ensure safety and good step coverage, a portion of the conductor is maintained at the conventional thickness ($\approx 5000\text{\AA}$):

In summary, three variations of the initial system concept were introduced during the course of the program. The first variation, a packaging of devices, was done for expediency, and has no relevance to the final system concept. The second and third variations are design improvements and Section 6 includes them in the final system definition.

Section 3

3.0 SYSTEM DESCRIPTION: CID ARRAY DESIGN

3.0.1 Cell Layout

Figure 3-1 shows the $30 \times 30 \mu\text{m}$ cell layout of the 128×128 sensor. The thick-thin oxide boundary is dashed, the lower conductor (N-doped-polysilicon) crosshatched, and the upper level (N-doped polysilicon) conductor is shown in solid outline. The lower level poly-thin oxide capacitor has an area of $1.36 \times 10^{-6} \text{ cm}^2$ and the upper level poly-thin oxide capacitor has an area of $1.81 \times 10^{-6} \text{ cm}^2$. Since the upper level capacitor has a thicker dielectric than the lower level capacitor, the charge storage capacity of each electrode is approximately the same, 1.9×10^6 carriers. Depletion capacitance loading limits the maximum output charge to 1.5×10^6 carriers.

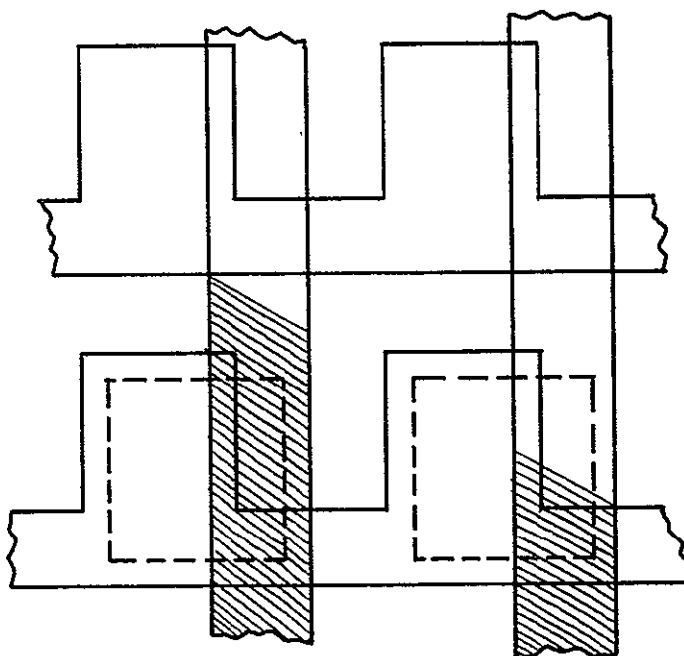


Figure 3-1. Cell Layout

3.0.2 Array Layout

The array in Figure 3-2 contains 128 rows and 128 columns, selected by groups of four on both the horizontal and vertical axes. Since the design of this array was for sequential readout of the image subblocks, selection is by means of scanning registers. In operation, a logical "one" would be entered into each scanning register and shifted, as required, to select the desired subgroup. The column drive lines, E_1 through E_4 , would then be driven to obtain four parallel outputs.

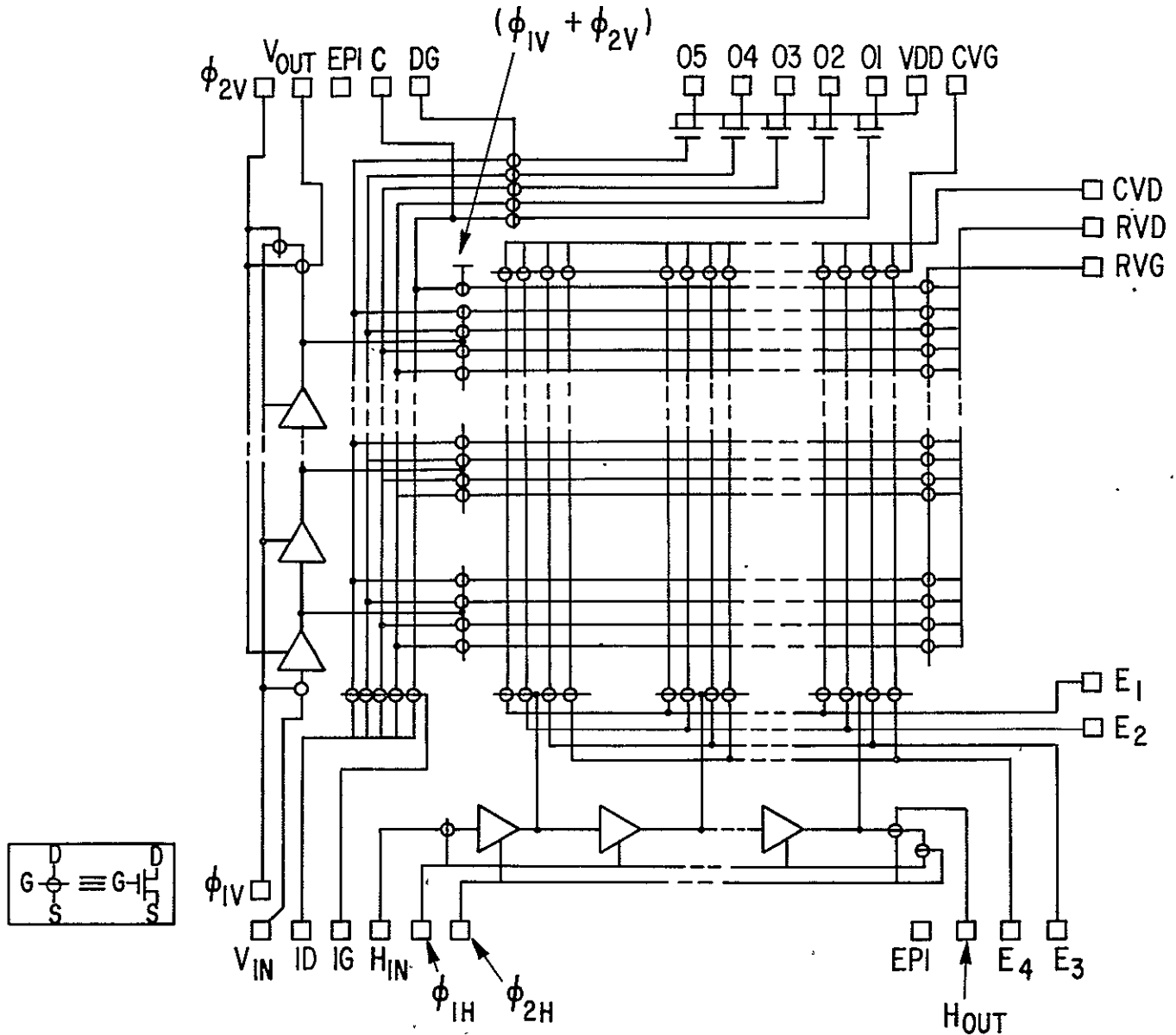


Figure 3-2. Sensor Layout

In addition to the 128 active rows, another row is available to provide differential cancellation of column drive interference. This compensation row is selected for every row address and is cleared when every row is cleared.

Overall chip size is approximately 5 x 5 mm. Figure 3-3 shows a photomicrograph of the array.

3.0.3 Array Parameters

Table 3-1 shows the calculated array electrical parameters for the 128 x 128 format.

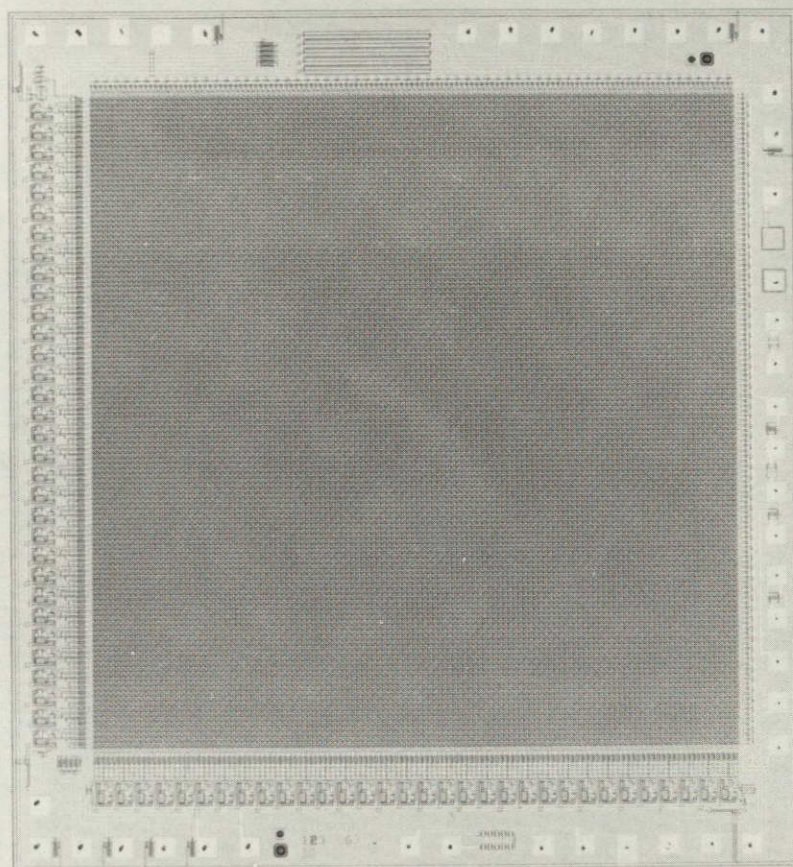


Figure 3-3. Array Photomicrograph

Table 3-1
ELECTRICAL PARAMETERS

Cell Storage Capacity	1.9×10^6 carriers
Saturation Output Charge	1.5×10^6 carriers (.24 pC)
Distributed Row Capacitance (C_{ROW})	6 pF
Sense Line Capacitance (C_S)	12 pF
Distributed Row Resistance	3.9 K Ω
Row Select Transistor Resistance	4 K Ω

3.1 READOUT METHOD

The readout technique for the track mode noise evaluation is the "double read" method described by Howard (1). As Figure 3-4 illustrates, a 4 x 4

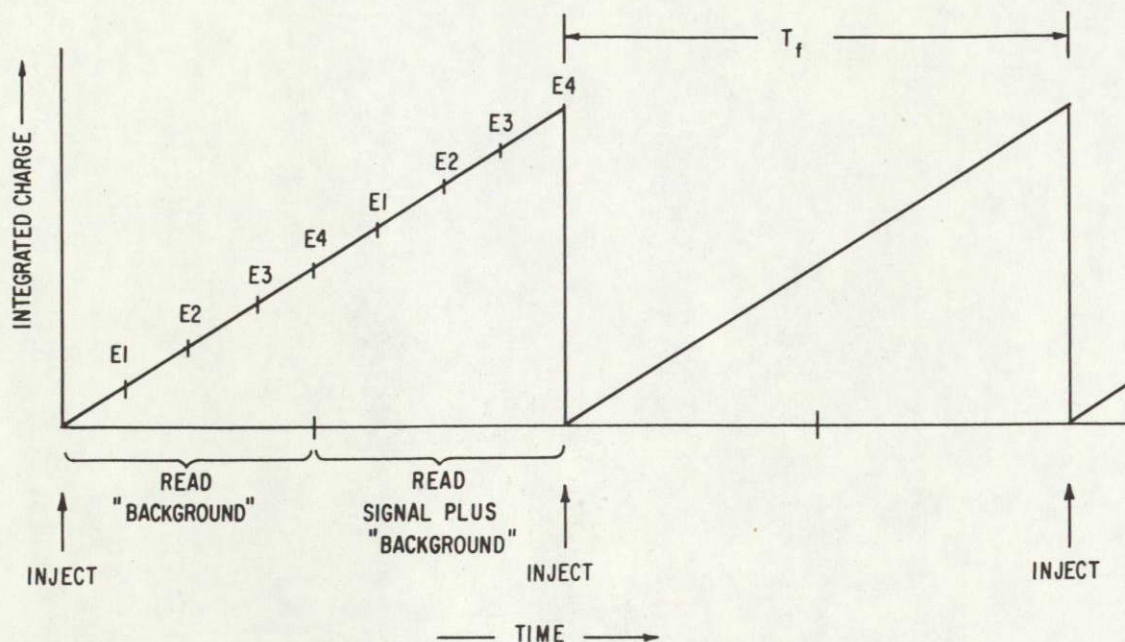


Figure 3-4. Track Mode Background Rejection Technique

pixel group is read out twice, non-destructively, and the first (background) group subtracted from the second group to form the net signal. This scheme effectively cancels the unwanted background signal (pattern noise) which repeats for each reading; however, a penalty is incurred because signal integration time is halved and Johnson noise increases. These effects will be discussed in more detail below. There are other approaches for background removal that could be implemented with less noise penalty. These, however, involve system considerations that could not be adequately evaluated under this program. It was decided to conduct the evaluation in this environment which unequivocally addresses the pattern noise concern even though the resulting signal-to-thermal noise ratio is degraded.

The noise performance to be reported here was obtained using the conventional sequential (block code) readout of the individual pixels. Hadamard and other transform readout methods were not employed. Transform readout remains an option for future designs where system operating characteristics are better defined and/or the need for a further reduction in system thermal noise is obvious.

3.2 CIRCUIT DESCRIPTION

Figure 3-5 shows a block diagram of the complete control and signal processing system. All control and timing waveforms were computer generated; and the same computer, using a separate program, processed the stored video data, calculated noise levels, etc.

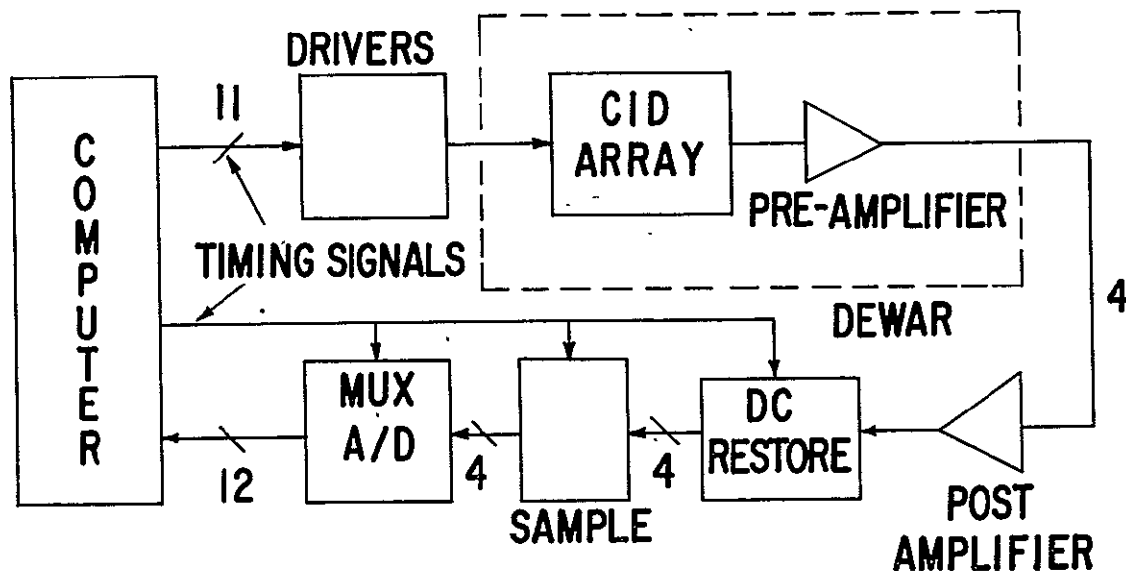


Figure 3-5. System Block Diagram

3.2.1 Preamplifier Circuit

Since amplifier noise is a significant factor in the overall noise inventory, the design of this function is critical to system performance. Particularly for the star tracker application, low frequency ($1/f$) noise is a concern. Therefore, on-chip MOS devices were discarded for off-chip J-FET's as input devices. The latter exhibit significantly lower noise at low frequencies, although their use increases input capacitance. The particular choice (2n6451) depended on the availability of these devices in chip form for mounting in the array package, and on the drain-to-gate leakage. Later changes in packaging and operating strategies subsequently disposed of both requirements; however, the program schedule did not permit circuit redesign.

A schematic diagram of the preamplifier circuit is shown in Figure 3-6. The input transistors operate as common-drain (source-follower) amplifiers. The outputs of these devices are dc coupled to bipolar differential-pairs which form the difference taking function between the compensation line and each of the four signal lines. A final stage operational amplifier provided double-ended to single-ended conversion of the amplified difference signals. Direct coupling was used throughout to avoid the problems associated with the use of coupling capacitors in the low impedance, low frequency environment.

In addition to the design of the basic preamplifier circuitry, great care was exercised in the design of peripheral circuitry, such as power supplies and biasing networks, to avoid contamination of the signal with excess thermal and induced noise from these sources. Finally, care was taken in the use of electronic instrumentation, including the data acquisition and computational circuitry, to minimize the noise contribution of the 60 Hz power lines.

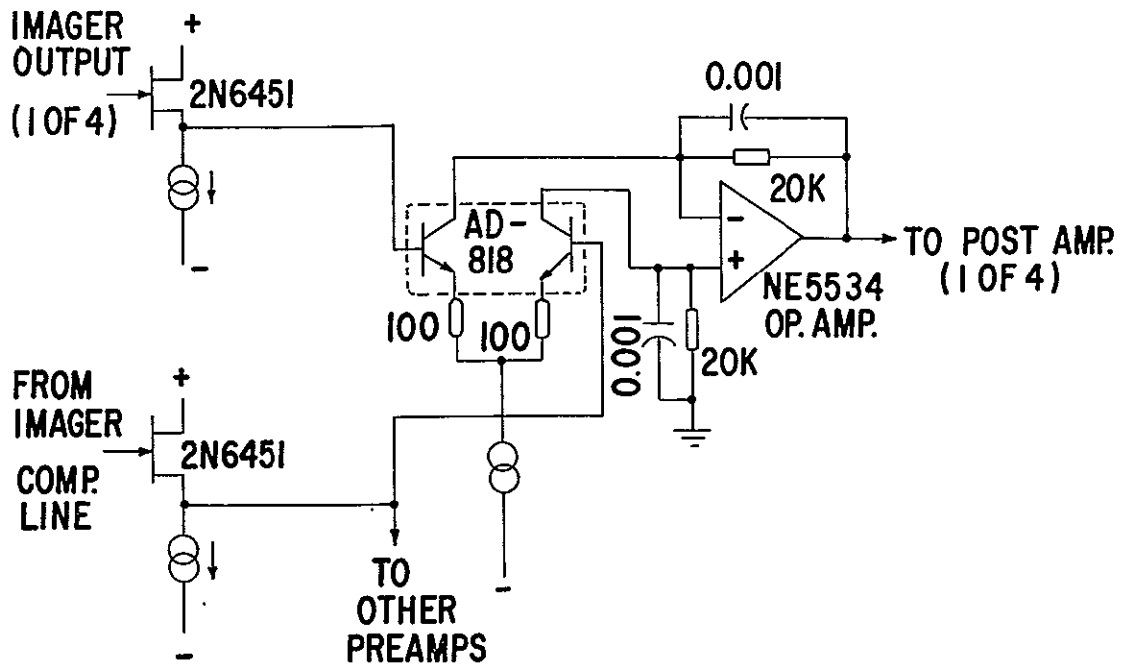


Figure 3-6. Preamplifier Schematic

3.2.2 Post Amplifier

The signal level after preamplification is high enough so that conventional data acquisition circuitry can function without significant contribution to the overall system noise. As Figure 3-7 shows, this circuitry consists of variable gain stage, used primarily to balance the gain of the individual channels, and two sample-and-hold circuits. In effect, the first S/H performs the restore function, while the second device samples the video signal and holds it for multiplexing into the A/D converter (not shown).

3.3 TIMING WAVEFORM GENERATION

The timing waveforms needed to drive the array in the "double read" method were sufficiently slow so that an assembly language program written for a 4 MHz Z-80 microcomputer could deliver all necessary signals at the proper times. A block diagram of the microcomputer, Figure 3-8, shows that the 11 digital signals required for array operation are sent to the driver board by outputting an 8-bit number to 1 of 3 latched parallel output ports of the Z-80 system. Thus, 11 of the 24 available bits are used for array timing. The drivers and voltage regulators on the driver board converted these TTL level signals to the appropriate MOS levels. Some of the other available bits are used directly for functions such as restore, sample and hold, A/D conversion, and sync pulses for the oscilloscope.

Figure 3-9 shows the general timing waveforms used in the "double read" method. The four columns in the 4 x 4 block are read sequentially, while the four rows are processed in parallel. After injection, each column is read for background and then 50 ms later it is read again for background plus signal. The first reading is subtracted from the second so that each column sees only 50 ms of signal integration time.

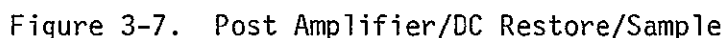


Figure 3-11 shows the read sequence in detail. In actuality, every time the computer reads a column, as per Figure 3-11, it reads that column 64 times and averages the readings. This method minimizes the leakage current component of noise in comparison to the other noise sources. It also allows the amplifier to be used beyond its $1/f$ noise region. This will be explained further in Section 4.

77

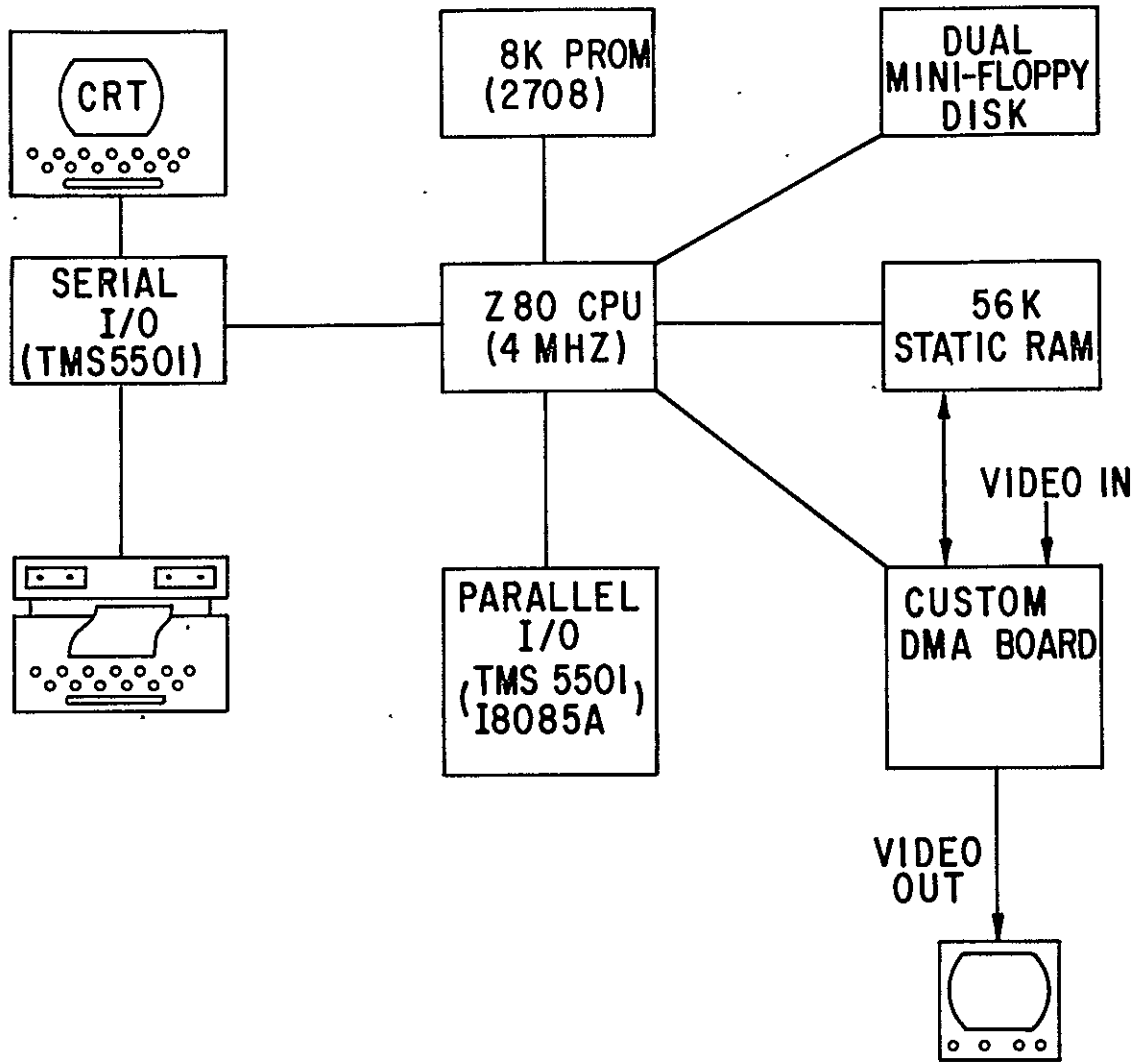


Figure 3-8. Microcomputer Block Diagram

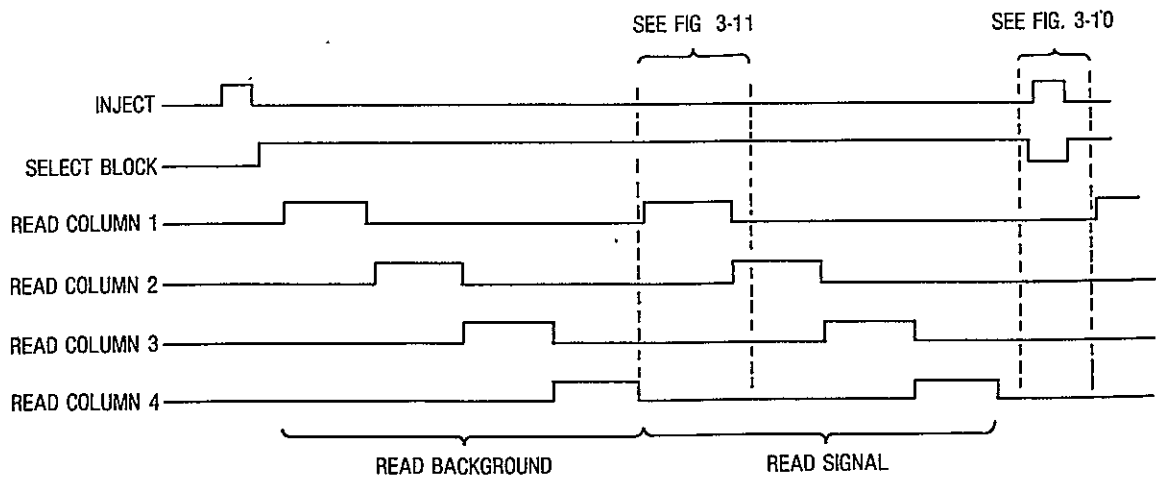


Figure 3-9. Overall Timing Diagram

STAR TRACKER TIMING DIAGRAM
INJECTION SEQUENCE

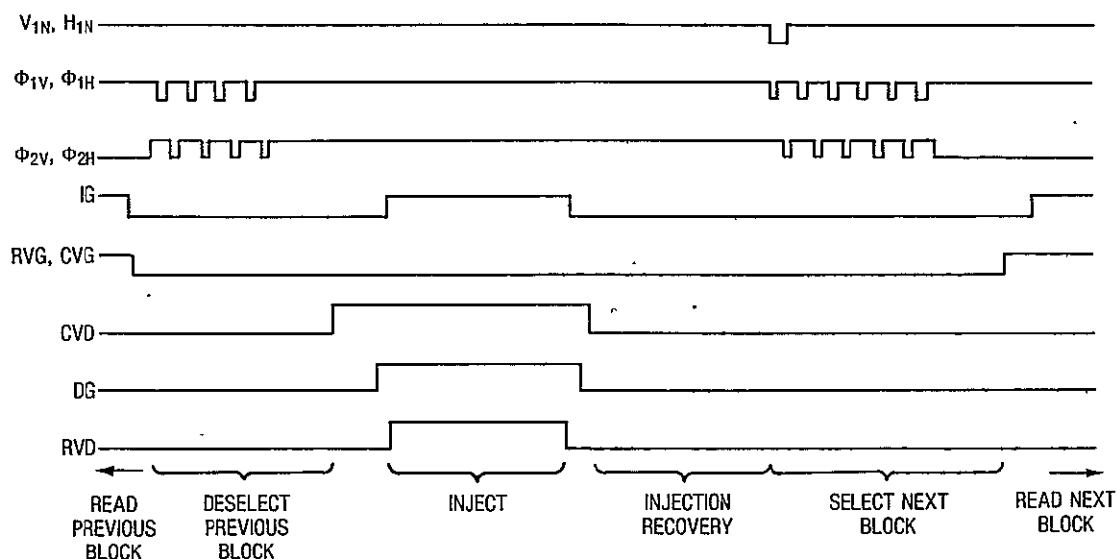


Figure 3-10. Timing Diagram-Injection Sequence

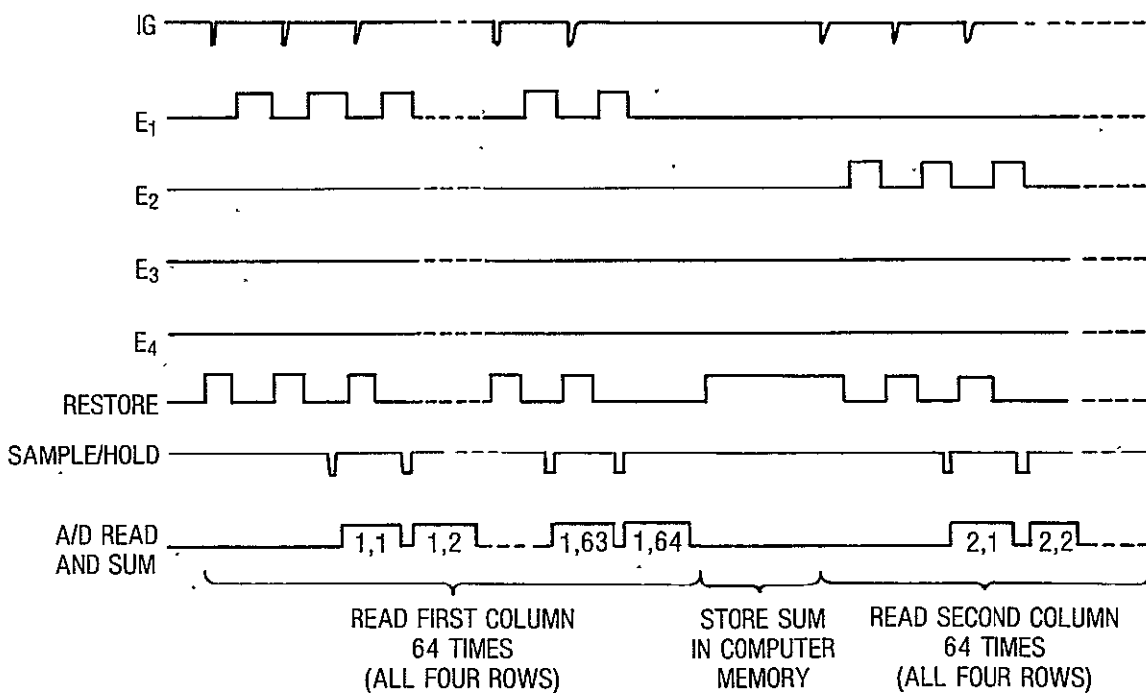


Figure 3-11. Timing Diagram-Read Sequence

one initial "dummy" reading is used but not processed in order to avoid start-up transients. After one column is read 64 times, the average reading for each of the four rows is stored in computer memory and the next column is read.

3.4 DATA COLLECTION AND PROCESSING

The Z-80 microcomputer collects and processes data and provides the timing waveforms for the star tracker. A 12-bit A/D converter module with an 8-channel differential-input multiplexer, buffer amplifier, and sample-and-hold circuit is used at its maximum throughput rate of 100 kHz. After the sample is taken and held for the four rows of each reading, the computer reads the four rows by sequentially updating the multiplexer channel and making conversions.

The computer stores an 18-bit sum of the sixty-four 12-bit readings for each pixel in the 4 x 4 group, for both the background and background-plus-signal. The 18-bit difference is then stored in the proper location in memory. We have determined that the converter quantization noise is insignificant as long as the RMS value of the noise to be measured is greater than, or equal to, the value of one least significant bit of the converter. For our setup, this LSB corresponded to 200 carriers. Another advantage of averaging 64 readings is that the noise on the average is $(64)^{1/2}$ or 8 times less than the noise on the individual readings. As a result, we can obtain the precision of a 15-bit converter while using only 12 bits. The difference taking adds a factor of $\sqrt{2}$ to the noise, since the noise adds incoherently. Thus one can measure noise levels as low as 35 carriers RMS with no significant quantization noise contribution.

Several versions of the computer program were written to perform the various tests. One version read out the whole array, a 4 x 4 block at a time, and stored the result in memory so that it could be displayed on a television monitor using the direct memory access display board shown in Figure 3-8. It was possible to simultaneously store and display two pictures, each containing an arbitrary 8-bit section of the 18-bit difference computed for each pixel. For example, one could show the most significant eight bits when a star was imaged or the next eight bits when the lens were closed, in order to see the background fixed pattern noise. This allowed a visualization of the tremendous dynamic range provided by the star tracker.

Another version of the program was written to measure the temporal noise level. This program chose the center block of the imager and read the block 100 times, storing the result each time for each of the 16 pixels in the block. A separate program, written in BASIC, calculated the mean and standard deviation (or RMS noise) for each pixel. Since the sample variance decreases linearly with the number of readings, the RMS error on these noise readings is 5%. Finally the program takes the average mean and standard deviation over the 16 pixels, thus reducing the error. These are the numbers that the noise analysis section quotes.

For the total noise measurement (fixed pattern and temporal noise) a slight variation was made in the temporal noise program. In this case 100 different blocks around the array were read and stored, and the same BASIC program was used to analyze the data.

Figure 3-12 shows a typical printout of total and temporal noise, respectively.

```

G40
OK
RUN
MEAN (CARRIERS)
 3173.39      1441.04      1217.21      802.576
 2885.05      1396.61      1186.9       791.048
 1635.07      1142.34      1063.71      683.925
 240.669      843.119      1008.01      561.13

RMS NOISE (CARRIERS)
 61.4902      49.07       48.5868      49.3299
 77.7592      49.9601      44.5927      48.1946
 82.1058      87.4405      45.7418      39.0117
 110.252      47.6229      45.1488      46.9341

AVG MEAN      AVG NOISE
 1254.49      58.3276
OK

Z80-MONITOR
>GC400

G40
OK
RUN
MEAN (CARRIERS)
 3122.48      1421.61      1182.62      783.146
 2855.13      1406.06      1182.75      783.535
 1573.03      1106.2       1048.56      695.713
 114.247      795.322      970.967      544.679

RMS NOISE (CARRIERS)
 39.7357      38.1496      34.3202      37.2071
 38.4948      40.5612      47.6798      34.8103
 39.7571      35.0289      32.3828      35.3801
 35.1439      36.2183      32.3066      37.5677

AVG MEAN      AVG NOISE
 1224.13      37.1715
OK

Z80-MONITOR
>GD000

```

Figure 3-12. Typical Noise Data Printout

3.5 TEST FIXTURE DESCRIPTION

All tests were carried out and data taken with the imager and preamplifier mounted in a demountable liquid nitrogen dewar (Infrared Laboratories

Inc., Model HD-2). Temperature of the dewar work surface was maintained by a controlled flow of chilled dry nitrogen into the dewar in place of the normal procedure of using liquid nitrogen directly. The dry nitrogen was cooled by heat exchange from a supply of liquid nitrogen in an open dewar, and the array temperature was monitored by a digital thermometer via a thermocouple attached to the imager package. Drive circuitry and post amplifier circuits were mounted on the dewar assembly and wired to the internal circuitry through hermetic connectors. An optical window in the dewar wall permitted the imaging of a light spot for verification of proper system operation. Figure 3-13 is a photograph of the complete system.

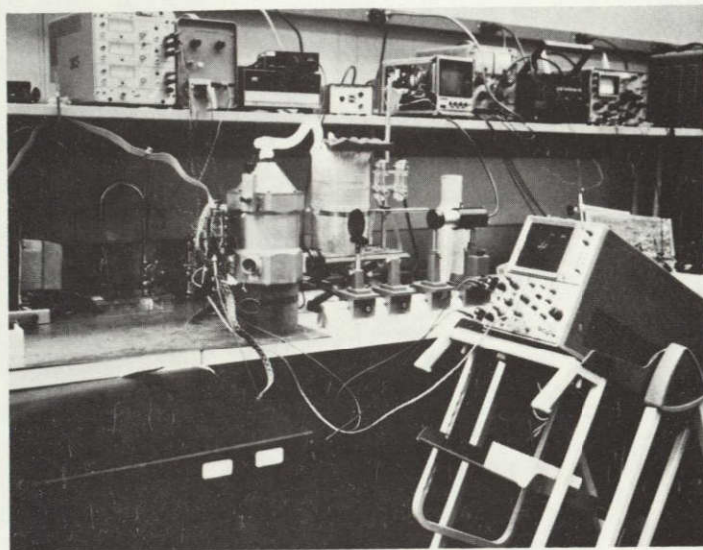


Figure 3-13. Test System Photograph

Section 4

4.0 NOISE PERFORMANCE

The circuitry used to select and provide readout of CID image sensors contains a number of Johnson noise sources. The distributed resistance of the array lines used for signal sensing, the line selection switch, and the first preamplifier stage each contribute temporal noise to the video signal. In addition, capacitor reset noise (KTC noise), shot noise in the dark current, and/or junction leakage current in the MOS line select multiplexers can be significant under certain conditions.

If a switch is used to set the voltage across a capacitor, thermal noise in the resistance of the switch results in an uncertainty in the final capacitor voltage. The magnitude of this uncertainty [3] is

$$V_n = (KT/C)^{1/2} \quad (5)$$

or

$$Q_n = (KTC)^{1/2} \quad (6)$$

where K = Boltzmann's constant = 1.38×10^{-23} W-s/°K and T = temperature in degrees Kelvin. It is possible to reference the charge signal to the input capacitor voltage after reset has been completed. This technique, called correlated double sampling results in the substitution of KTC noise on a clamping capacitor for KTC noise on the array output capacitance. The level of KTC noise referred to the array can be made arbitrarily small, however, since gain can be used between the array output and the clamp capacitor. Voltage noise at the input of the preamplifier results in an equivalent input charge that is directly proportional to the array output capacitance ($q = cv$). Theoretical preamplifier noise levels of a few hundred carriers result from array output capacitance levels in the 10-pF region.

Under low video rate readout conditions, Johnson noise can be minimized by restricting the noise bandwidth of the video amplifier. Shot noise originating in array dark current and line select multiplexer junction leakage can be limiting under these conditions. Reductions in array operating temperature can control these thermally generated currents and, consequently, the resultant shot noise.

4.1 THEORETICAL TEMPORAL NOISE LEVELS

The theoretical levels of the significant noise sources in CID image sensors have been investigated and experimentally verified in a detailed noise study.⁽⁴⁾ The significant temporal noise sources encountered in an array operating in a star-tracking mode are defined below:

- a) Distributed Row Resistance

$$N_{DR} = (4KTBR_R/3)^{1/2} C_R/q$$

where N_{DR} = rms noise equivalent carriers
 K = Boltzmann's Constant
 T = absolute temperature
 B = noise bandwidth
 R_R = row resistance
 C_R = row capacitance
 q = electronic charge

b) Row Select Switch

$$N_{RS} = (4KTBR_S)^{1/2} C_R / q$$

where N_{RS} = rms noise equivalent carriers
 R_S = Row Select Switch resistance

The channel resistance of an MOS switch, R_C , is given by:

$$R_C = 1 / (\mu C_O (W/L) (V_{gs} - V_t))$$

where μ = carrier mobility
 C_O = oxide capacitance
 W = channel width
 L = channel length
 V_{gs} = gate-source voltage
 V_t = threshold voltage

Parasitic source and drain resistance resulting from the non-zero sheet resistance of the transistor source and drain region must be added to the channel resistance, R_C , to obtain total selection switch resistance, R_S .

c) KTC Noise

$$N_{KTC} = (KTC_F)^{1/2} / q = 401 C_p^{1/2}$$

where N_{KTC} = rms noise carriers
 C_F = capacitance, Farads
 C_p = capacitance, pico Farads

The degree to which KTC noise is suppressed by correlated double sampling is determined by the degree to which the first sample is a measure of the KTC offset voltage. For a video system whose bandwidth is limited by a single time constant, the magnitude of the sample voltage is:

$$V_{\text{sample}} = V_{\text{signal}} (1 - e^{-T/RC})$$

If the sample interval, T , is made to equal 4 time constants, then $V_{\text{sample}}/V_{\text{signal}} = 0.98$. In this case, KTC noise would be suppressed by a factor of 50.

d) Amplifier Noise

The equivalent noise resistance of a junction FET is:

$$R_a = 2/(3 g_m)$$

where

g_m = transistor transconductance

The amplifier noise is given by:

$$N_a = (4KTBR_a)^{1/2} C_t / q$$

where

N_a = rms noise carriers

R_a = Transistor noise resistance

C_t = Total input capacitance

e) Junction Leakage Current Shot Noise

$$N_j = (I_{j1} t_s / q)^{1/2}$$

where

N_{j1} = RMS noise carriers

I_{j1} = junction leakage current

t_s = sample time interval

f) Dark Current Shot Noise

$$N_D = (I_D t_i / q)^{1/2}$$

where

N_D = RMS noise carriers

I_D = dark current per pixel

t_i = integration time interval

Table 4-1 lists the theoretical noise levels for the FPP-128 array operated in this star tracker evaluation camera.

Table 4-1
THEORETICAL NOISE LEVEL

Source	Spot Noise ($\text{nV}/\text{Hz}^{1/2}$)	Effective Capacitance (pf)	Noise Level (carriers/ $\text{Hz}^{1/2}$)
Row Resistance ($5\text{K}\Omega$)	5.2	6.0	0.20
Row Select Switch ($3\text{K}\Omega$)	7.0	6.0	0.26
Disconnect Switch ($2.4\text{K}\Omega$)	6.3	10.4	0.41
J-FET Preamplifier	1.1	31.0	0.21 *
Differential Amplifier (per input)	1.9	31.0	0.37 *
Root Mean Square			0.68

*Theoretical RMS Amplifier Noise (0.43) compares with measured value of 0.57)

The video amplifiers operated with a bandwidth limiting time constant of 20 microseconds. This gives a noise bandwidth of $B = (\pi/2)(1/2\pi RC) = 12.5 \text{ kHz}$. Correlated double sampling results in the addition of amplifier noise power for each of the two samples, effectively doubling the noise bandwidth to 25 KHz. Each of the two correlated sample intervals were set at 4 time constants ($80 \mu\text{s}$) to suppress KTC noise by a factor of 50. Leakage current shot noise was negligible over this sample time interval.

4.1.1 Low Frequency Operation

The dominant temporal noise at high video rates is from Johnson noise sources (resistors, switches, field effect transistors). As the operating frequency is reduced a reduction in Johnson noise, proportional to the square root of bandwidth, can be realized. At lower rates, however, low frequency excess noise and leakage current begin to interfere with the sensing operation. It would appear that these low frequency noise effects would dominate below some video rate and limit the improvement which this approach could achieve. This is not the case, however. There is a strategy that allows these low frequency effects to be circumvented and the effective noise bandwidth to be reduced with, at this writing, no known limit.

The strategy is to choose the imager operating frequency for lowest noise, somewhat above the point where low frequency effects become significant, and then use multiple non-destructive readout operations and external signal summation to further reduce the effective noise bandwidth. Because signals sum coherently and uncorrelated noise incoherently, the effective noise is reduced in proportion to the square root of the number of non-destructive readout operations. This strategy is effective in reducing all temporally uncorrelated noise, including Johnson noise, KTC noise, charge transfer noise, and leakage current shot noise.

4.2 FIXED PATTERN NOISE

Solid-state image sensors can exhibit a fixed non-uniform spatial background in the reproduced image. The major sources of fixed pattern noise in CID image sensors are transistor switching interference, array photolithographic variations, bias charge variations, and silicon material defects.

One particular silicon material defect that could affect tracking accuracy is resistivity striations in the single crystals grown from the molten state.⁽⁵⁾ These striations could lead to lateral movement of photon-generated charge between the location from which it generated and the pixel storage region. The use of more uniformly doped epitaxially grown silicon or transmutation-doped silicon should avoid this potential problem, which is common to all silicon image sensing devices. Non-uniform coupling of the MOS transistor scanner output voltage to the video signal results in a component of fixed pattern noise that repeats from scan to scan. Variations in row-to-column crossover capacitance arising from either insulator thickness or photolithographic variations cause a two dimensional component of fixed pattern noise. Variations in the bias charge from site-to-site, caused by differences in storage capacitance or threshold voltage, also result in a two-dimensional component of fixed pattern noise. Differential sensing and signal processing can minimize these effects.

Dark current non-uniformity can be an important source of pattern noise, particularly at room temperature. The inherently low dark current performance of CID imagers is an advantage under these conditions.

Site-to-site variations in sensitivity will result in the appearance of FPN which is more pronounced in the highlight portion of the image. This effect could be the result of patterning variations in any opaque or semi-opaque layers on the array surface. In some instances, this might result from gain differences of amplifier channels that are subsequently multiplexed onto a single video line. The latter cause can be corrected by suitable adjustment, and is not considered a fundamental FPN source. Sensitivity variations of the FPP-128 array were measured by first finding the mean signal for 25 readings at 3/4 full-scale illumination for each of 50 sites along a row. Similar values, measured for no illumination, were subtracted from these values. The 49 differences of these signal-minus-background values were then averaged to determine the pixel-to-pixel sensitivity variation. Measured sensitivity variations of 1/2 percent are typical for these imagers. Thus, the FPN contribution of sensitivity variations is relatively small.

4.3 MEASURED RESULTS

Temporal noise was measured as a function of temperature with the imager operating in the track mode. In this operational mode a 4 x 4 sub-group of pixels is read out twice each frame. The difference between these two readouts is taken to cancel fixed pattern noise. An integration time of 50 ms results from this procedure, with the imager operating at 10 frames per second. A single 4 x 4 sub-group was read out 100 times at each temperature

setting and the standard deviation of the readings for each pixel was calculated. The average of the 16 resultant standard deviations is plotted as the temporal noise level at each temperature.

Total noise was measured by reading a single frame for each of 100 different 4 x 4 sub-groups distributed over the image sensor. The standard deviation was calculated for each pixel of the 4 x 4 sub-group. The average of the 16 resultant standard deviations is plotted as the total noise level at each temperature.

Figure 4-1 shows the temporal and total noise measured on three arrays from wafer #9-7. This wafer exhibited high dark current which is responsible for the high total noise observed. The spatial variation in dark current gives rise to a pattern noise which varies with temperature in the same manner as the dark current itself, which decreases by a factor of two for each 8°C reduction in temperature. Shot noise associated with this dark current is proportional to the square root of the quantity of dark charge collected and consequently is reduced by a factor of 2 for every 16°C reduction in temperature. This effect can be seen in the temporal noise data for imager #9-7-15. Figure 4-2 represents results obtained with arrays from a wafer with the proper dark current level. Dark current shot noise is lower than the Johnson noise level of 40 carriers for temperatures below 5°C. The spatial variation of dark current, the dominant fixed pattern noise at room temperature, is lower than other fixed pattern noise components at 0°C. The increase in total noise at very low temperature is a fixed pattern effect caused by the scanning registers. It is believed that certain scanner circuit nodes, which do not have their voltage levels well-controlled, caused the effect. This effect can be avoided with a different scanner design or with a digital decoder for row and column selection.

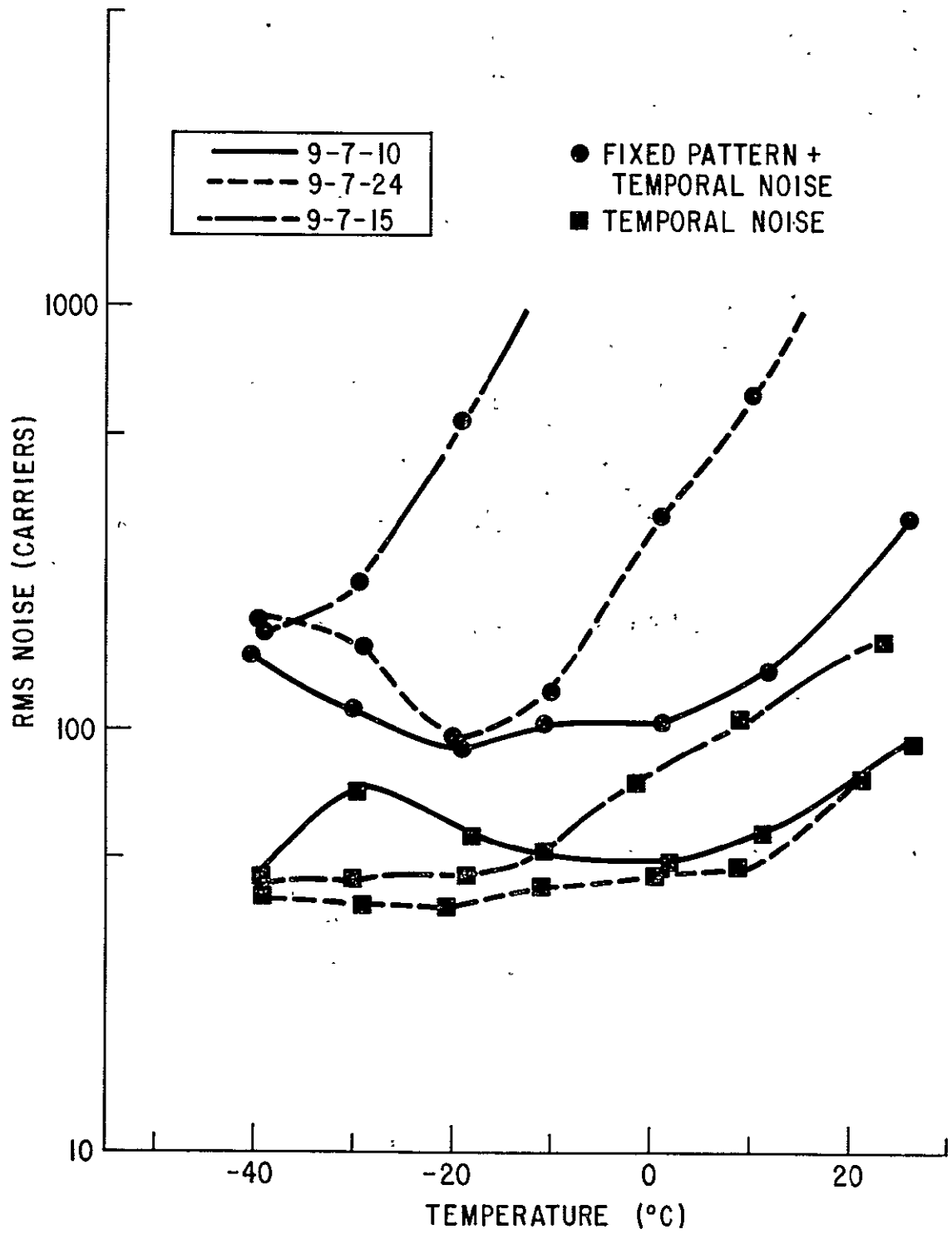


Figure 4-1. Measured Noise-Wafer #7

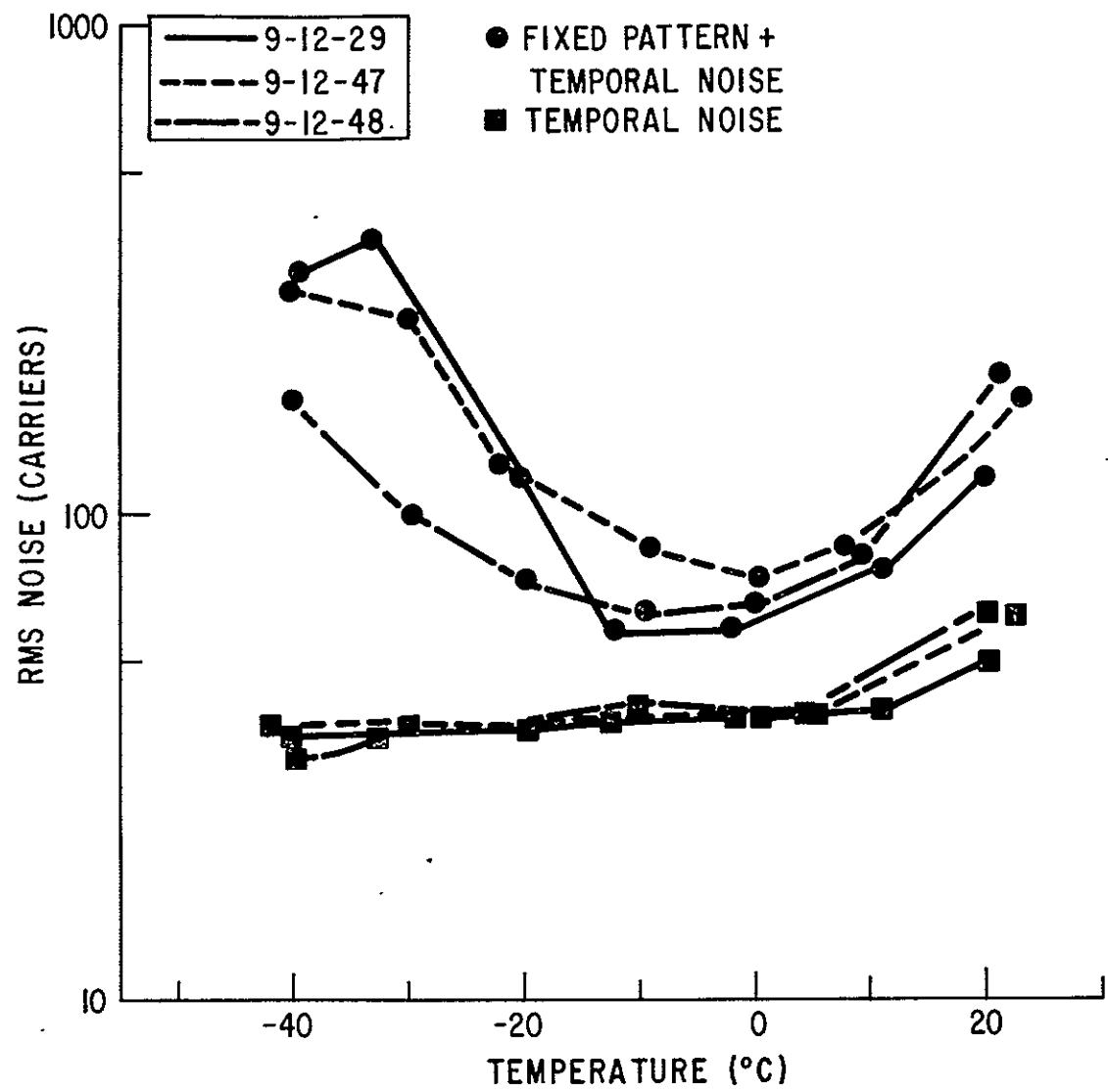


Figure 4-2. Measured Noise-Wafer #12

Section 5

5.0 SPECTRAL RESPONSE/QUANTUM YIELD

In the following presentation, the term "quantum efficiency" refers to the ratio of charge collected to incident optical photons (see Figure 5-1). In sensing this stored charge in a CID imager, a loss is incurred due to the charge lost in restoring the depletion region under the storage electrode after injection. For the subject device, the factor was 0.82. Here the term "quantum yield" will describe the ratio of detected charge to incident photons. As indicated in Figure 5-1, any additional gain losses are considered part of the overall system gain.

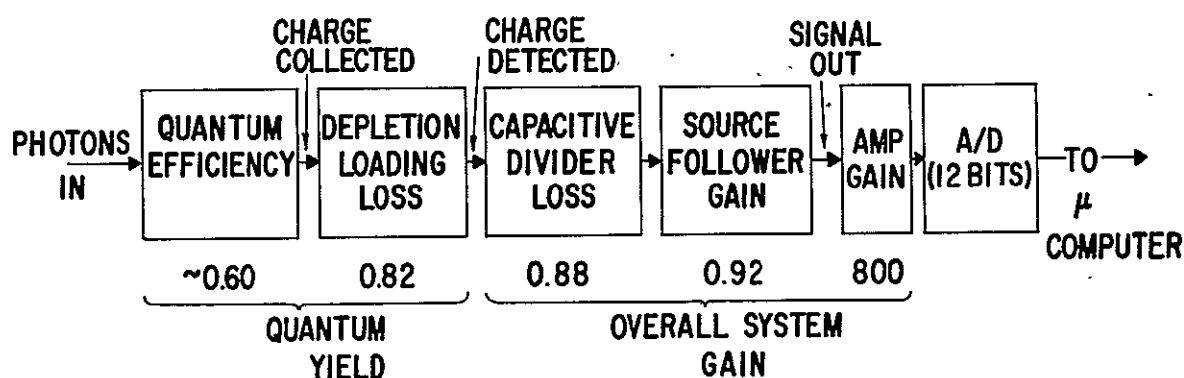


Figure 5-1. Signal Flow Diagram

The data that follow are presented in terms of quantum yield in order that it be referenced to the same point in the signal chain as the noise data presented above.

5.1 MEASURED RESULTS

The quantum yield of six imagers having thin polysilicon upper electrodes was measured over the spectral range of 0.41 to 1.05 μm at room temperature. Each imager was also cooled while measuring quantum yield at .8 μm to evaluate any temperature effects on imager spectral performance.

Measurements were made by placing the imager in an evacuated dewar and illuminating the array through a dewar window with light from a constant energy glass prism monochromator (Perkin Elmer Model 98). At the imager location a silicon photo diode (GE #E07) measured incident light power per unit area at each functioning wavelength. An NBS calibration (Test #212736) determined its absolute spectral response.

During charge sensing, electronics located outside the dewar maintained all row and column electrode voltages at -10V. This permitted simultaneous collection of photo-generated charge at each sensing site in the array. The value of the resulting substrate current was used to calculate quantum yield, which is defined as the ratio of the number of electrons read from the imager to the number of incident photons.

Results of the quantum yield measurements for imagers from wafer #9-7 and #9-12, appear in Figures 5-2 and 5-3 respectively. The average quantum yield of the six devices is 24% at .41 μm and above 45% from .6 to .95 μm .

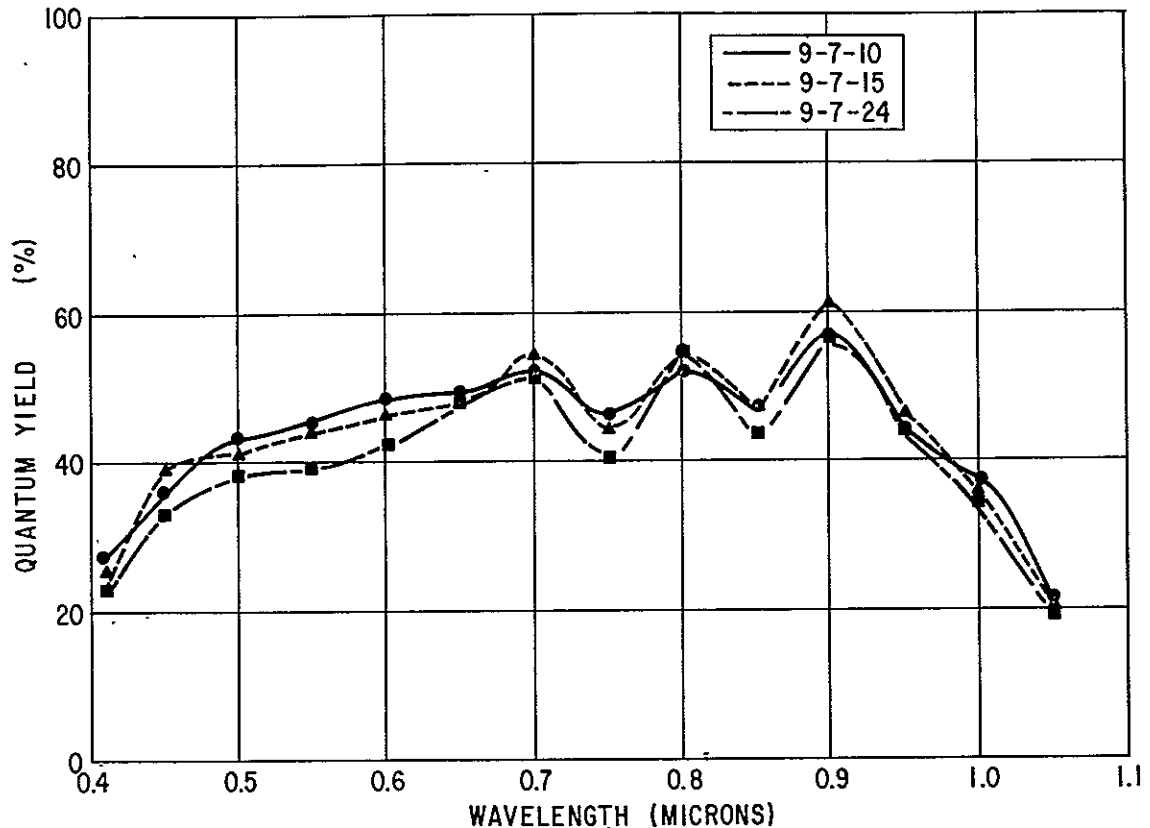


Figure 5-2. Quantum Yield vs Wavelength: Wafer #7

Quantum yield measurements were also made for imagers having ATO upper electrodes. At corresponding wavelengths, the ATO imagers have a 5-25% lower QY than the thin polysilicon imagers.

Failure of the transparent electrode material to produce higher quantum efficiencies cannot be accounted for, but an excessive charge recombination rate at the silicon surface could be responsible.

5.2 TEMPERATURE EFFECTS

Cooling the imagers to -20°C produced no measurable change in quantum yield at .8 μm . However, studies of the silicon energy absorption curve at 77°K (-196°C) by Dash and Newman⁽⁶⁾ show a temperature coefficient of the bandgap of about $-4 \times 10^{-4} \text{ eV}/^{\circ}\text{C}$. These data suggest that the quantum yield curves in Figures 5-2 and 5-3 would show a significant leftward shift if measured at 77°K (-196°C). The shift would be more pronounced at longer wavelengths, decreasing QY by 30% at 1.0 μm ; but the shift would have little effect at wavelengths shorter than .85 μm . Over the temperature range of -20 to $+25^{\circ}\text{C}$; however, this effect is negligible.

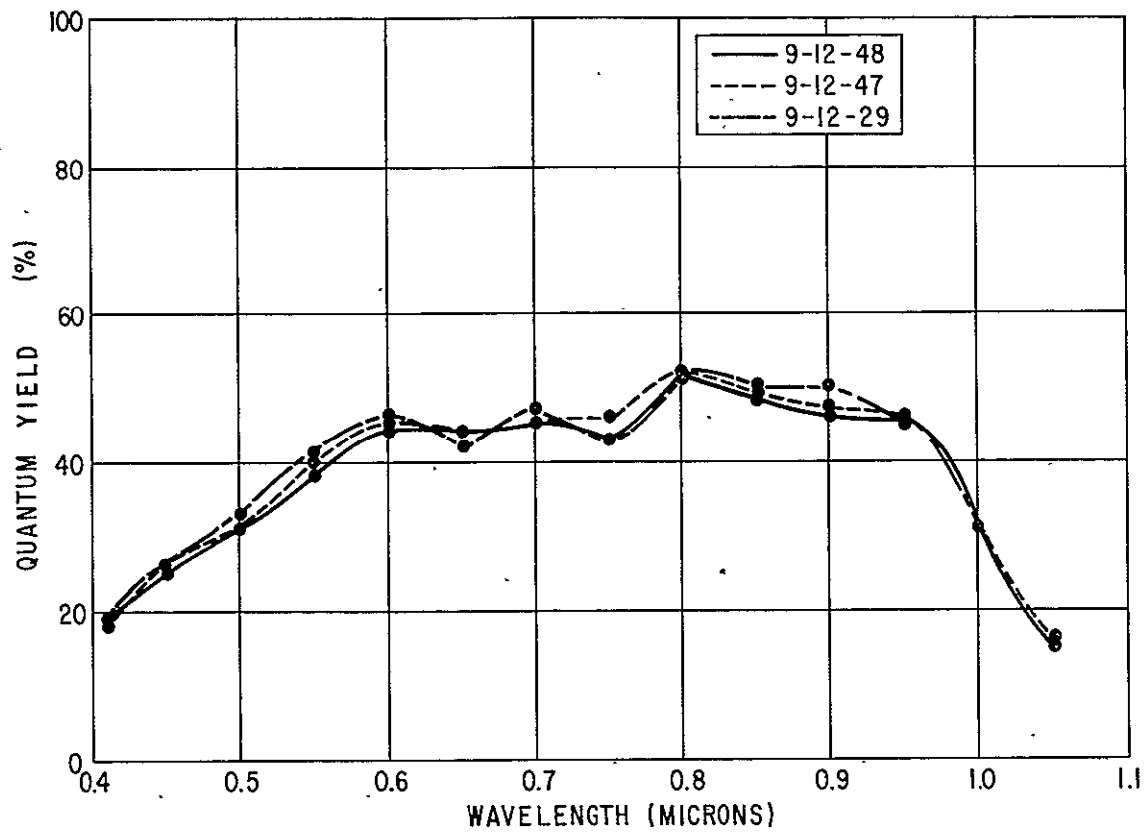


Figure 5-3. Quantum Yield vs Wavelength: Wafer #12

Section 6

6.0 PROJECTED PERFORMANCE OF LARGE ARRAY

Projecting the performance of the 128 x 128 test array to an array of order of 400 x 400 involves more than simply proportionally scaling the test array parameters to those of a larger device, because the larger device would differ significantly from the test array in both design and level of technology. In addition, changes in readout methods and circuitry would affect final performance.

While at this time the actual configuration of the 400 x 400 array's selection techniques, tracking sub-group size, and other system-related details is uncertain, some changes in design are clearly indicated. The unneeded "disconnect" transistor, a major noise source in the test device, would be eliminated and capacitive coupling between the signal lines and compensation line would be reduced. A symmetrical cell layout is also desirable to minimize signal irregularities caused by photomask mis-registrations. Finally, improvements in processing technology would reduce the sensing site size and, hence, overall chip size. A 20 μ m square sensing site size, for instance, would result in a 8 x 8 mm sensing area with the overall chip size being only slightly larger. This size chip could be processed with high confidence and with excellent projected performance as will be detailed below. It should be noted that this choice of array size, in the absence of specific system requirements, is somewhat arbitrary. From a system perspective, the preference is for a large number of sensing sites. In a multi-array system, there will be a trade-off decision among the number of arrays, array cost, and complexity of manufacture. The results derived here can be considered a reference point for any final system decisions.

6.1 NOISE

As discussed in Section 4, each on-chip noise source must be considered in relation to the effective capacitance upon which it operates in order to assess its contribution to total noise charge. It is necessary, therefore, to calculate both the resistance and capacitance of the new design in order to establish new theoretical noise values. Using this approach, the noise contributions of the four major noise sources were computed and tabulated in Table 6-1. It was assumed that double sampling and cooling significantly reduced KTC noise and leakage current shot noise. Column 1 of Table 6.1 lists the baseline values for the 128 x 128 test array. The noise contributions of the on-chip sources are nominal values extrapolated from measurements of appropriate test devices. The test fixture directly measured preamplifier noise and a total of approximately 10 noise equivalent carriers (NEC) per channel of the input differential preamplifier was computed. This count yields a total measured value of about 28 NEC as measured in the test fixture, because a noise multiplier of $2(2)^{1/2}$ is incurred in the various differencing operations inherent in the readout method used. (Actual measured values, as reported in Section 4, were on the order of 36 NEC.)

Table 6.1
THEORETICAL NOISE/CHANNEL
FOR 400 x 400 ARRAY FOR DIFFERENT DESIGN CONDITIONS

Noise Source	128 x 128 Baseline (NEC/ $\sqrt{\text{Hz}}$)	400 x 400 (NEC/ $\sqrt{\text{Hz}}$)	400 x 400 (rows strapped) (NEC/ $\sqrt{\text{Hz}}$)	400 x 400 (N-Channel process) (NEC/ $\sqrt{\text{Hz}}$)
Row Resistance	0.20	0.75	0.0	0.0
Row Select Transistor	0.25	0.30	0.4	0.22
Disconnect Transistor	0.44	0.0	0.0	0.0
Pre-Amplifier	0.57	0.21	0.21	0.21
Total Spot Noise	0.79	0.84	0.45	0.30
Total Noise (@ B.W. = 150 Hz)	9.7 NEC	10.2 NEC	5.5 NEC	3.7 NEC

Column 2 of Table 6.1 gives the equivalent values for the 400 x 400 array. These numbers reflect not only the effects of scaling, but also the effects of actions which can correct deficiencies in the test structure. Detailed examination of Column 2 reveals that the noise contribution of the distributed row resistance has increased significantly due to an increase in its effective resistance and capacitance. The larger row capacitance also raised the noise charge of the row select transistor. The so-called "disconnect transistor," an unneeded feature, is presumed eliminated, and the preamplifier noise reduced, the latter by the improved circuit design and the signal-averaging readout method. This method permits a higher sampling rate. The net result of about 11 NEC per channel is only slightly different from that of the test device, an encouraging result.

The dominance of the row resistance component of this noise, however, leads one to consider the possibility of reducing that effect. The application of a conductive "strap" to the offending conductor can virtually eliminate this resistance. Column 3 of Table 6.1 gives the result of this action. Because of layout constraints, row capacitance must be increased slightly, and this change adversely affects the noise charge associated with the row select transistor. In addition, some obscuration of the incident radiation would occur (about 12.5%). In view of the trade-off considerations involved, this feature might best be considered a design option.

Finally, Column 4 reflects the further noise reduction possible with the addition of N-channel processing, currently under development at General Electric. The viability of this development depends on program timing for any projected application. Because of program timing and the realization that an attempt to physically attain the indicated noise level would require a re-appraisal of many noise sources now considered negligible, Column 4 results are discounted in the system evaluation to follow.

Section 7

7.0 SYSTEM STUDY RESULTS

The application studies covered in this section of the report were supplementary efforts to cover the CID's performance when used in stellar sensor applications. The requirements for several stellar sensor applications were considered. However, the Space Telescope FGS was selected as a basis for identifying the range of sensor application since it provides the best example of the three primary modes of operation, namely, acquisition, tracking and astrometry. General Electric has already done significant work on the star tracker application.⁽¹⁾ This report also considers the use of the CID sensor, with an emphasis on the acquisition mode and further evaluation of the track and astrometry modes.

The net results of the application studies shows the CID continues to hold excellent promise for star tracker applications because of its unique characteristics. The CID baseline design characteristics are shown in Table 7-1.

Table 7-1
CID BASE LINE DESIGN

1. Chip Size	400 x 400
2. Pixel Subtense (arc-s)	0.5
3. Pixel Size (μm)	20 x 20
4. Total Active Area (mm)	8.0 x 8.0
5. Site Storage Capacity (carriers)	10^6
6. Effective Capacity (carriers)	8×10^5
7. Estimated NEC (carriers)	25

The results of the requirements analysis task show that the specific readout technique used, and its impact on the detail chip design, should be selected through a specific set of requirements in order to demonstrate the performance advantages of the CID in general and a selected design in particular. The different readout techniques can be incorporated into the chip design with high confidence once the device is adequately characterized.

7.1 REQUIREMENTS SUMMARY

Representative stellar sensor requirements were examined for five potential applications for the CID sensor. These applications included the Fine Guidance Sensor (FGS) for the Space Telescope, the Fixed Head Stellar Tracker (FHST), and a representative booster inertial navigation system update case. The results of this review are shown in Table 7-2 where the parameters of interest are tabulated for comparison purposes. It is cautioned

PRECEDING PAGE BLANK NOT FILMED 32

Table 7-2
SUMMARY COMPARISON OF REPRESENTATIVE STAR TRACKER REQUIREMENTS
NOISE MODELS

Key Parameters	FGS/S.T.			FHST		STELLAR	HAADS	Booster INS Update
	Aca.	Track	Astr.	Acq.	Track	Acq./Track		
1. FOV	109 min ² (multi chip)		20 min ²	Total 8.5 ⁰	8 ⁰ x 8 ⁰	2 ⁰	8 ⁰	1 ⁰ x 1 ⁰
2. Prob. of Det. %	85	-	-	95	-	-	95	-
3. Visual Mag. (M _V)	7 - 14	7 - 14	7 - 21	2 - 5.7 Gov	2 - 5.7 Gov			1 - 3
4. Eff. Aper. Dia (cm)	200			5.8		-	2.5	-
5. LOS Rate arc-s	<2	<0.2	<.2	<1000	<1000	-	6.8 to 285	neg.
6. Min. Data Rate (Hz)	-	20	1 Meg Bits/s	-	-	3 to 10	>1/hr.	2.6
7. Integration (s) Times	>.22	.025	.050 to 600	-	-	-	-	.04
8. Acq. Time (s)	60	-	-	10	-	0.2	-	-
9. Pos. Acc. (arc-s)	0.5	.01(1σ)	.01(1σ)	-	180 (uncal) 10 (1σ)	1.7	1.0 (Bias)	~1
10. Stability (arc-s)	-	.0028 (1σ)	.0028 (1σ)	-	16 for M _V = 5.7 7.3 for M _V	0.1 to 0.7 M _V = 6	1.7 RMS	-
11. Mag. Acc. (%)	-	-	1	-	-	-	12.5	-

that the numbers shown were taken from a variety of sources and have not been fully verified in terms of their interpretation or their accuracy. For this reason a number should be considered as identifying representative ranges of interest rather than specifications for the application shown.

For the cases shown, the tightest accuracy and stability specifications are for the Fine Guidance Sensor. In practice, the difficulty of meeting accuracy requirements is a function of the pixel or chip field of view. The numbers can be selected arbitrarily based on either the number of pixels per chip or the number of chips used to cover the desired field of view.

In considering the signal level for a variety of applications, a combination of several factors must be considered. The principal ones involve the effective aperture size, the magnitude of the star to be detected, and the integration time available, which is limited by the line-of-sight rate and the selected subtense angle of the pixel. A comparison has been made of the worst case signal level which might be expected for three of the applications shown in Table 7-2. The results are shown in Table 7-3 and indicate two limiting cases of interest. The first case shown is that in which the integration time is limited by the pixel subtense angle divided by the line-of-sight rate. The most stringent requirement shown would be the High Altitude Attitude Demonstration System (HAADS) where the signal level is one the order of one-tenth of the signal level in the Space Telescope acquisition mode because of the field of view and high spin rate (LOS rate). However, if the data frame rate is selected as the limiting time interval, the signal for the FGS acquisition mode is about the same as HAADS. The signal levels shown for the astrometry mode can be selected based on the desired integration time and hence do not represent a limiting case. These figures indicate that for sensitivity as well as accuracy, the FGS is the most stringent requirement. Hence, in the analyses which follow, the FGS for the Space Telescope requirements has been used as a basis for the application potential of the CID. A summary of the assumed requirements for each of the three modes is presented in Figure 7-1.

Table 7-3
REPRESENTATIVE WORST CASE REQUIREMENTS

App./Mode	Eff. Ap.Dia (cm)	Pixel Sub Tense (arc-s)	Visual Mag. (m_v)	Los Rate Limited t_i^* (s)	Relative Signal Strength	Frame Rate Limited (s)	Relative Signal Strength
Space Tel/Acq.	200	.5	14	.25	1	.025	0.1
Space Tel/Track	200	.5	14	2.5	10	.025	1.0
Fhst/Track	5.8	60	6	.07	.3	-	-
**HAADS/Track	2.5	60	7	.25	.1	-	-

$$*t_i = \frac{\theta}{\text{LOS}}$$

**HAADS = USAF - High Altitude Attitude Determination System

7.2 NOISE MODELS

The noise model assumed for these analyses identifies the predominant noise sources and is based on extrapolating the test data for the 128 x 128 chip to a 400 X 400 chip design, as presented in Section 6. The resulting noise models are tabulated in Table 7-4.

ACQUISITION MODE

- Full Frame Scan
- M_V 14 Star Acquisition
- 2 arc-s/s Initial Angular Velocity
- 0.5 arc-s Error After Acquisition
- 60 s Acquisition Time
- No Angular Rate Measurement Available

TRACK MODE

- M_V 7 to M_V 14 Stars
- 0.01 arc-s Accuracy
- .0028 arc-s Stability
- 20 Hz Frame Rate
- 0.2 arc-s/s Maximum Line-of-Sight Rate
- 5 Star Tracks Simultaneously

ASTROMETRY

- M_V 10 to 17 (and Dimmer ~ Goal of $M_V = 21$)
- Integration Time 50 MS to 600 s
- Separate Stars as Close as 0.1 to 1 arc-s
- Magnitude Accuracy 1% for $M_V = 17$
- Dump All Data in Minimum Time ~ Typically 2.6 s

Figure 7-1. Baseline Requirements

Table 7-4
NOISE SUMMARY

Source	Noise, NEC*
1. Thermal Noise	$N_t = 2.0 t_r^{-1/2}$, t_r = total read time for 1 pixel (64 samples)
2. Dark Current Shot Noise	$N_{ds} = 51 t_i^{1/2}$, t_i = time from inject to sample
3. Dark Current Pattern Noise	$N_{dp} = 350 t_i$, t_i = time from inject to sample
4. Leakage Current Shot Noise	$N_{ls} = 25 t_r^{1/2}$, t_r = time from reset to sample
5. Fixed Pattern Noise	$N_{fp} = 2.2 \times 10^4$ Can be suppressed by double-read technique to negligible levels
6. KTC Noise	$N_{ktc} = 5$ Suppressed by correlated double sampling and multiple read techniques from 1800 NEC

*NEC = Noise equivalent carriers, rms, after on-chip differencing, before frame-to-frame differencing.

7.3 ACQUISITION MODE

The purpose of the Acquisition Mode is to reduce the initial state of image position uncertainty and velocity to a state which is compatible with handover to the Tracking Mode. The Acquisition Mode may also be used to acquire a second guide star after a slewing command has caused loss of track of a first guide star. In this case, a reasonably rapid acquisition will be required. The handover state will be achieved by reduction of the errors through interaction of the guide sensor, the inertial reference, and the attitude control system.

The initial state will depend on characteristics of the ACS and inertial reference which are not defined. However, it is assumed that significant errors in both velocity and position will be present.

A worst case is assumed on the status of the attitude control at the beginning of acquisition, whereby the ACS is started up after a period of dormancy and the inertial attitude reference is degraded to the point where a full frame acquisition scan is needed to assure acquisition of a suitable target star. If the initial attitude is random, there may be no bright star in the viewfield.

During the period of dormancy, the vehicle may have accumulated a significant angular velocity. It may be desirable to perform an acquisition before stabilizing the vehicle with the aid of an inertial rate reference. These assumptions lead to the following set of initial acquisition requirements:

- Full frame scan
- M_V 14 star acquisition
- Initial angular velocity - 2 arc-s/s
- Final acquisition error 0.5 arc-s after 60 s
- No rate measurement available

These requirements constitute a worst case situation, but will be used to demonstrate how the system can be reactivated after a period of dormancy or possibly after partial failure of the inertial reference.

7.3.1 Effect of Image Velocity

The integrated signal charge per pixel is inversely proportional to the image velocity:

$$N_{SP} = \frac{\theta_p \dot{N}_s}{2 \dot{\theta}}, \text{ where} \quad (1)$$

θ_p = pixel subtense angle (0.5 arc-s)

\dot{N}_s = signal charge generation rate (1.4×10^5 e/s, $M_V = 14$),

$\dot{\theta}$ = line-of-sight rate (arc-s/s)

and the factor of 2 allows for the image being split on 2 pixels. N_{sp} may vary with the orientation of the image track relative to the pixel structure. The maximum per pixel signal charge will be achieved when the image has moved a distance equal to two pixel subtenses, or in an integration time

$$t_e = \frac{2 \theta p}{\dot{\theta}} \quad (2)$$

7.3.2 Effect of Position Error

The initial scan area must be large enough to assure acquisition of a detectable star. The density of stars brighter than $M_V 14$ is at least 100 per square degree (galactic pole). Each 400×400 pixel sensor subtends $(400 \times 0.5)^2 = 40,000$ square arc-s, and six sensors will see an average of

$$\frac{40,000 \times 6 \times 100}{(3600)^2} \approx 2 \text{ stars @ } M_V 14$$

To assure acquisition in random orientation, each sensor should therefore execute a full frame scan.

7.3.3 Frame Time

Consider a full frame scan including a double read operation to cancel fixed pattern noise. If we were to read out each 4×4 group as one pixel, then the full frame time would be

$$\begin{aligned} t_f &= 2 \times 100 \times 100 t_r + t_e, \text{ where} \\ t_r &= \text{per pixel read time} \\ t_e &= \text{added time to expose before start of readout} \end{aligned} \quad (3)$$

and two read operations are executed per pixel. For the more critical case of high image velocity, the exposure time would be relatively short so that t_e could be neglected in (3).

The noise model of Table 7-4 provides noise estimates in terms of per pixel read time, t_r , and time since injection, t_i . These estimates are based on single site readout and must be adjusted to accommodate the new condition of 4×4 group readout. The corrections are

- thermal noise x 2 increase
- dark current shot noise x 4 increase
- dark current pattern noise x 1 increase
- leakage shot noise x 2 increase

and result from the fact that a summation of four rows, each consisting of four pixels, would be taken. Thus the signal Σ would contain $(4)^{1/2} = 2$ times as much thermal and leakage shot noise and $(16)^{1/2} = 4$ times as much dark current shot noise as an individual pixel. It is more difficult to assess

the multiplier for the dark current pattern noise since it is not, in general, randomly distributed pixel-to-pixel. High spatial frequency pattern noise would be averaged while low spatial frequency components would be less affected. A multiplier of unity was assumed for this analysis. The reset noise and fixed pattern noise components are assumed to be made negligible and are disregarded in this analysis.

In a frame comprising two read operations per pixel, two thermal and two leakage noise samples sum incoherently, but only one sample of dark current pattern noise and shot noise is obtained, since the dark charge is injected before the second read operation. The total per pixel noise (16 sites) is:

$$N_t^2 = \left(\frac{2\sqrt{2} (2)}{(t_r)^{1/2}} \right)^2 + \left(2\sqrt{2} (25) t_r^{1/2} \right)^2 + \left(51 \times 4 t_i^{1/2} \right)^2 + \left(350 t_i \right)^2$$

Substituting t_f from (3) and neglecting t_e ,

$$N_t^2 = 64 \times 10^4 / t_f + 5000 t_f / (2 \times 10^4) + 4.16 \times 10^4 t_i + 1.23 \times 10^5 t_i^2 \quad (4)$$

Equation (4) expresses per pixel noise in terms of frame time and time since injection. If a line is read out, then injected and re-read, the time since injection will equal the frame time.

From (1)

$$N_{sp} = 4 \theta_p N_s / 2 \dot{\theta} = 1.4 \times 10^5 t_f / \dot{\theta} \quad \text{and} \quad (5)$$

$$(S/N)^2 = \frac{2 \times 10^{10} t_f^2 / \dot{\theta}^2}{64 \times 10^4 / t_f + 4.16 \times 10^4 t_f + 1.23 \times 10^5 t_f^2} \quad (6)$$

$$\frac{S/N}{\dot{\theta}} = \frac{10^6 t_f^3}{32 + 2.08 t_f^2 + 6.15 t_f^3} \quad (7)$$

This expression has no maximum but increases with t_f . From (2); however, the maximum per pixel signal is reached when the image has traversed two pixel subtenses. In this case

$$t_f = 4 / \dot{\theta}, \text{ for maximum signal} \quad (8)$$

For $\dot{\theta} = 2$ arc-s/s, $t_f = 2$ s, in which case $S/N_4 = 149$ for a M_{14} star. The read rate for this condition would be $2 \text{ s} / 2 \times 10^4 = 100 \mu\text{s}$. Alternatively, one could operate at a fixed frame time of, say, one second. In this case the image would generate a track of length

$$\frac{\dot{\theta}}{4 \theta_p} = \dot{\theta} / 2 \text{ subgroups}$$

Thus if θ were high, the per pixel S/N would be low according to (7), but the number of opportunities for detection would be large. Under these conditions, it is likely that reliable detection could be achieved at angular velocities up to 8 arc-s/s, where S/N = 20. There would be 4 exposed groups in a frame.

The first scan would locate the target within a few groups, depending on the angular velocity. The next scan could be restricted to a smaller area, resulting in a shorter frame time and a more accurate position measurement. Depending on the characteristics of the ACS, hand over to track mode would be achieved in a few seconds.

7.4 TRACK MODE

For the track mode it is assumed that the system must be capable of handling a visual magnitude range of $M_V 7$ to $M_V 14$ and provide 0.01 arc-s accuracy and 0.0028 arc-s stability at a frame rate of at least 20 Hz. The maximum line-of-sight rate is unspecified but, for the sake of discussion, a LOS rate of 0.2 arc-s/s will be assumed, consistent with the rate specified by Stanton, et al.⁽⁷⁾ for solar system tracking. Capability must exist for tracking at least five stars either simultaneously or sequentially. Differences in the time of star centroid location must be accounted for if sequential tracking is used. The five star images will normally be expected to fall on five different arrays in order to avoid the penalty of increased readout bandwidth; however, should several star images fall on one array, the capability would exist for simultaneous tracking of five stars with concomitant bandwidth increase.

7.4.1 Accuracy/Stability

Tracking accuracy depends upon star visual magnitude, pixel subtense angle, pixel-to-pixel variations in sensitivity and linearity, system thermal noise, and star signal shot noise. Tracking stability is affected by all of the above except sensitivity and linearity variations. It is assumed that background variations (offsets) from pixel-to-pixel are reduced to an insignificant level by the double read method, the noise model is as given in Section 7.2, and the pixel subtense angle is 0.5 arc-s.

These effects are analyzed in the Appendix to find the accuracy and stability levels attainable. The limiting cases of thermal noise only, signal shot noise only, and linearity variations only, are analyzed for the star image centered on a 3 x 3 array and for the image located at the corner of the center pixel in a 3 x 3 array. The radius of stability (r_s) and radius of accuracy (r_A) derived from the calculations are restated below and plotted in Figure 7-2.

Case A1-Star centered, thermal noise only:

$$r_s = (2.02 \times 10^{-8})(2.5)^{M_V} \text{ arc-s} \quad (\text{A30})$$

Case A2-Star in corner, thermal noise only:

$$r_s = (2.65 \times 10^{-8})(2.5)^{M_V} \text{ arc-s} \quad (\text{A33})$$

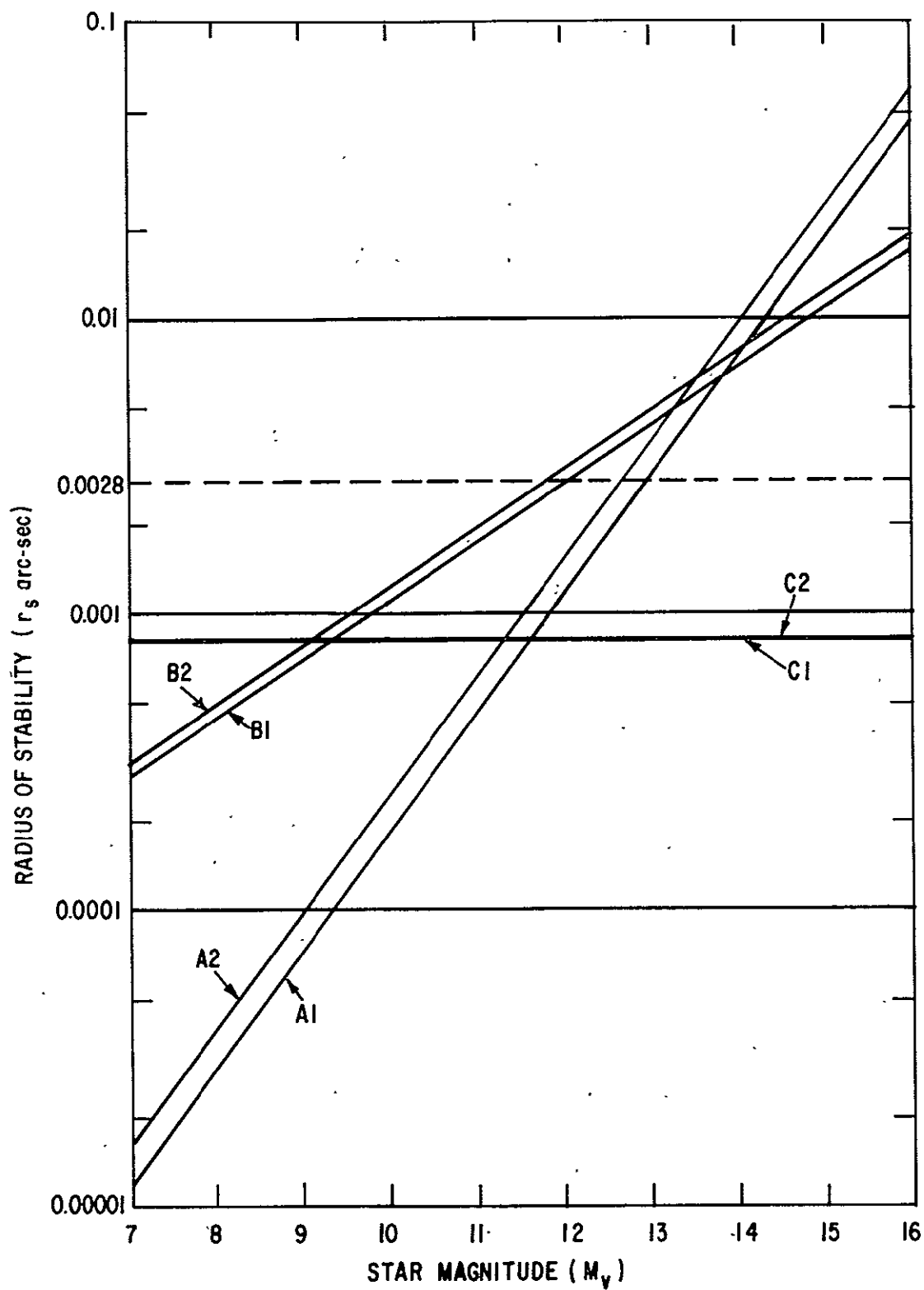


Figure 7-2. Radius of Stability Vs Star Magnitude

Case B1-Star centered, shot noise only:

$$r_s = (1.14 \times 10^{-5})(2.5)^{M_V/2} \text{ arc-s} \quad (\text{A37})$$

Case B2-Star in corner, shot noise only:

$$r_s = (1.23 \times 10^{-5})(2.5)^{M_V/2} \text{ arc-s} \quad (\text{A41})$$

Case C1-Star centered, linearity variations only:

$$r_A = .000828 \text{ arc-s} \quad (\text{A46})$$

Case C2-Star in corner, linearity variations only:

$$r_A = .000837 \text{ arc-s} \quad (\text{A49})$$

The curves of Figure 7-2 show that the specification of .0028 arc-s stability is actually limited to a star of visual magnitude $M_V \leq 12$ by the shot noise on the signal and not by system thermal noise. The linearity variations are an insignificant contribution to the radius of accuracy, and so the combined thermal noise and signal shot noise allow the .01 arc-s specification to be met by stars of magnitude $M_V \leq 14$.

7.4.2 Signal Integration Times

The required signal integration time depends upon the visual magnitude of the star to be tracked, the noise, and the desired S/N ratio for detection and tracking; or the noise level required for accurate magnitude determination. These parameters are shown in Figure 7-3 in order to highlight the perspective values involved for a given application. In Figure 7-3, the times required to attain given S/N ratios are plotted against stellar visual magnitude. Curve A shows the time required for saturation of the center pixel of a 3 x 3 pixel group, assuming a centered star image. Curves B, C, and D indicate the integration times required to attain S/N ratios of 1000, 100, and 10 respectively, at temperatures of 0 °C and -25 °C. These curves were generated using an approximate formula that includes the effect of system thermal noise, signal shot noise, and dark current shot noise. The thermal noise was assumed to be 25 carriers rms and the dark current was assumed to be 2 nA/cm² at 25 °C. The S/N values used for the calculations represent the total star signal divided by the noise on a single pixel, as defined for the centroid calculations.

It is seen from the curves in Figure 7-3, that system thermal noise is of significance only for integration times below about 0.1 second and low S/N ratios; otherwise shot noise predominates. Reducing array temperature below about 0 °C is seen to be useful only at the very long integration times.

With the required frame rate of 20 Hz, a S/N ratio of 10, and thermal noise level of 25 carriers, stars as dim as M_V 18 could be acquired and tracked with a radius of stability of about 0.2 arc-s. While it is valid to consider the reduction of system thermal noise below 25 carriers by several available techniques, such as transform readout, background signal storage, etc., the benefits would seem to be limited to the short integration times and low S/N ratio conditions.

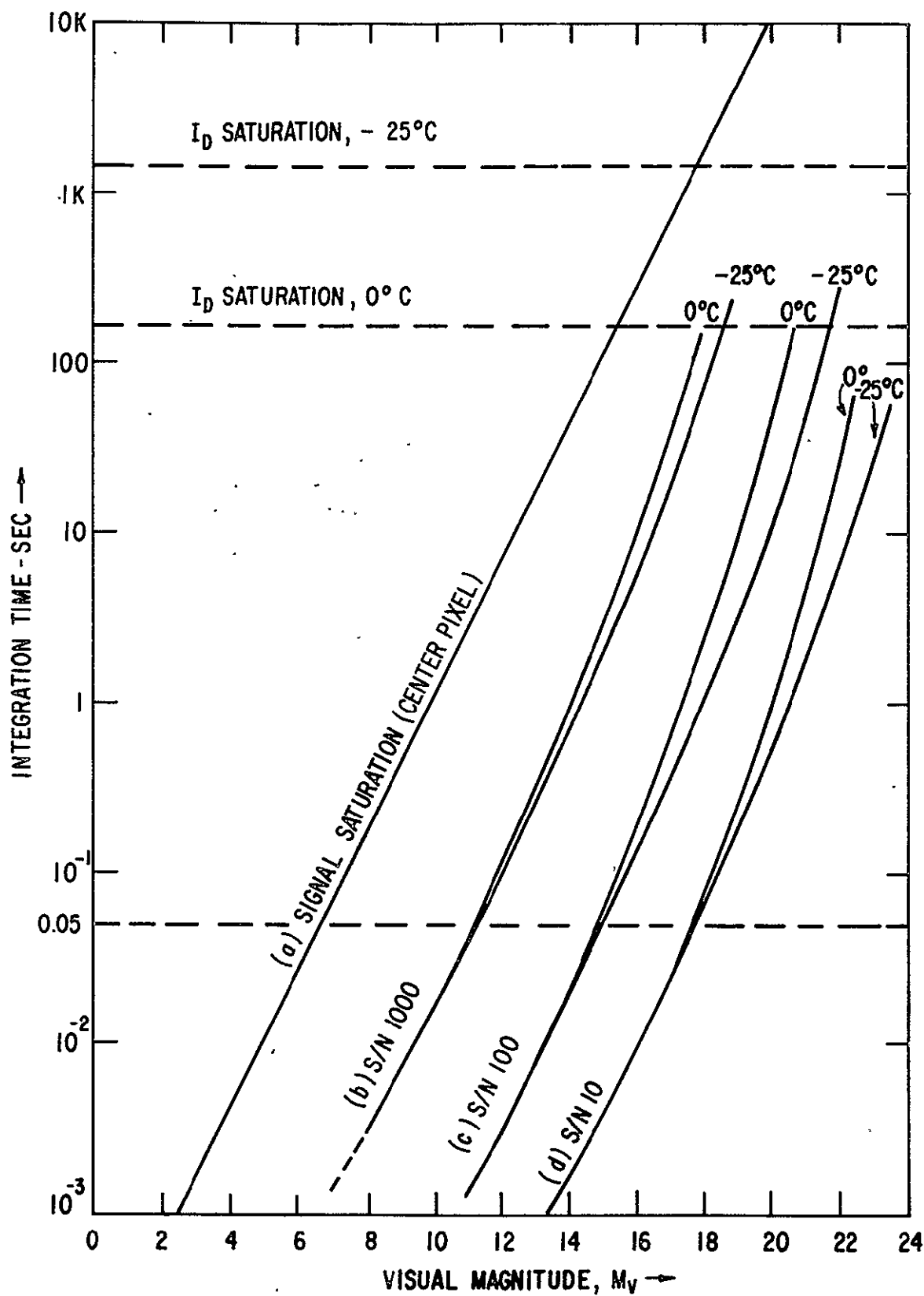


Figure 7-3. Integration Time Vs Visual Magnitude

The reader is reminded that the results indicated in Figure 7-3 are based on approximate numbers and are presented as a rough design tool and not for specification. When a detailed error analysis has been accomplished, this chart could serve as a guide for selecting operating modes. The possibility exists for automatic programming of integration times for optimum system performance.

Figure 7-3 also shows that integration times larger than 0.05 second would result in signal saturation of the center pixel for $M_V 7$ stars whereas $M_V 17$ stars would permit integration times on the order of 500 s before saturation occurred. For the longer times, array temperature would be a factor.

7.4.3 Implementation Approaches

The preceding section discussed the impact of the various performance and noise considerations on the system computations required. This section provides further detail on computation methods which may be implemented for the track mode. The selected method will depend on the particular detail requirements, but for an application where minimum noise is essential, the recommended method would be to use a 4×4 submatrix array with four parallel amplifiers as an output to reduce data rates and provide maximum flexibility for tracking multiple stars. The basic scheme would use correlated double sampling at an optimum sample rate selected to minimize leakage, KTC, and Johnson noise. Sixty-four samples would be accumulated for a given read time using the NDRO capability of the CID to enhance the signal-to-noise ratio. Digital double correlation would be used to reduce pattern noise by 60 db. A chip temperature of 0°C appears adequate for tracking up through $M_V 14$ stars, but for astrometry, further cooling is indicated. To determine if the stability goal of .0028 arc-s for $M_V 14$ stars could be met, further analysis is needed. It appears from the preceding analyses that the system would require a significant reduction of the 20 Hz frame data rate in order to permit sufficient integration time to achieve the necessary S/N ratio (≈ 1000) to meet the stated stability goal. The proposed mechanization can handle five stars, but with some further bandwidth penalty over a single star, unless further parallel outputting is used. A more detailed analysis and design effort is required to establish the specific mechanization.

One of the key features of the CID is the ability to randomly access individual pixels. The random access can be achieved by scanning registers on the chip or by using decoders to address a specific pixel in a shorter time period. The choice of one approach over the other again depends on the specific implementation requirements.

7.5 ASTROMETRY MODE

The astrometry mode is assumed to require a readout of stars of between $M_V 10$ and $M_V 17$ with a desirability of reading out up to $M_V 21$. Integration time requirements vary from a minimum of 50 ms to as long as 600 s, the maximum integration time required for a magnitude 21 star.

The system should be capable of separating stars spaced as close as 0.1 arc-s, and of determining magnitude to an accuracy of 1 percent for a $M_V 17$ star. Finally it should be capable of reading out all the pixels in 2.6 s, based on FGS requirements.

7.5.1 Variable Magnitude

The CID appears to be able to handle all of the star magnitudes indicated in the requirement. The dimmer stars may require additional cooling in order to avoid dark current saturation and to achieve accuracies for the magnitude required. The CID is unique in the fact that it is possible to allow the system to integrate while reading. Even if individual pixels saturate, those which are not saturated can be read.

7.5.2 Separation of Stars

The requirement indicates a desirability of separating stars as close as 0.1 arc-s. Based on the current design with a pixel of a half arc-s and typical blur circle approximately the same size, the presence of two stars one-tenth of an arc-s apart would cause a change in the size of the blur circle. It appears to be possible to measure this difference in the order of 20 percent and hence detect star separation in the order of 0.1 arc-s as is currently done with photographic emulsions.

7.5.3 Magnitude Accuracy

The requirement for 1% magnitude accuracy requires that the signal to noise be at least 100 after a multiple reading and that the sensor responsivity variations be 1% or less. This performance appears to be within the capabilities of the system. Figure 7-3 indicates that adequate signal to noise ratios appear to exist for star magnitude up to M 18. Pixel-to-pixel variations of <1 percent have been measured on representative arrays. If necessary, calibration could be used for the pixels of interest. All pixels could be stored in memory but this would take more memory than desired. In this case, selected subsets of the array could be useful if the vehicle maneuvered such that the stars of interest appear in these calibrated pixels.

7.5.4 Complete Array Dump

The requirement for reading all of the pixels in as short a time as possible has several ramifications. In the JPL report, (8) 2.6 s was used at a time to dump the charge in all pixels. If this were used for the 400 x 400 CID (.06 ms/pixel), it would increase the read rate over that for the track mode (.003 ms). The temporal noise would then be as large as 100 carriers for this rapid readout and hence loss of signal to noise would occur. An alternative is to read at the slower rate. It would take as long as 50 s to read all the pixels. If selected areas were read out, the time would be a function of the number of pixels involved. Several options exist as to how to read all of the data in the array.

7.5.5 Implementation

Based on the above discussion it appears that in the astrometry mode many of the techniques that have been discussed for the track mode would also be used. However, the main difference is that the readout rate requirement is open and increased integration times are acceptable. It is possible with the CID to continue integration after some pixels have saturated while simultaneously reading out other pixels of interest. This feature provides a major asset for the astrometry mode because of the ability to improve

dynamic range. Specifically, the pixels may be read out at a rate corresponding to a minimum noise rate. Repetitive reading will enhance accuracy and permit linearity measurements. The ability to read pixels at random allows one to keep track of background current, dark current, and variations in the star signals over the total integration time. This provides a unique CID capability.

The exact method of reading out the data to telemetry is a matter of the particular interface details. The JPL report (9) shows the use of two line buffers in order to store data prior to transmitting over the telemetry links. A similar approach would be anticipated for the CID but because of the ability to separate readout from integration, the readout times are not critical.

7.6 COMPUTER IMPLICATIONS

A brief review of the computational implications was made in order to assess the major areas of concern in implementing the computational algorithms. In general the primary forcing functions for the star trackers are in the readout rate areas and readout accuracies. The general problem of computer memory to store the required algorithms and to store data appears to be a relatively minor problem in light of the large memory capacity of existing technology. The computations required are relatively simple and have little impact on the throughput capacity of current microcomputers.

Typical numbers depend so much on the application that it is difficult to generalize. However, the JPL study of the Fine Guidance Sensor indicated on the order of 1,000 words of RAM and 1,000 words of PROM would be adequate. A similar study for a different application by Rockwell on a High Altitude Attitude Control Demonstration System (HAADS) utilized a fairly complex fit pattern threshold calculation and stored a great deal of data in order to minimize this dark current bias correction factor. In this case a random access memory of 4,000 words and a PROM memory of 4,000 words was required. A brief look of the Fine Guidance System and the computations that we would anticipate for most applications, indicate that a maximum of 4,000 words of RAM and 4,000 words of PROM memory are all that would normally be required except where excessive amounts of calibration of individual pixel data are desired. For example, if in the case of a 500 x 500 pixel array, all pixels were to be calibrated with an 8 bit word this would require 250,000 words, 2×10^6 bits. Using today's technology, 64,000 bits on a single chip are reasonable ROM memory. In this case, the amount of memory would take about 30 chips which is a relatively small hardware penalty.

The accuracy requirements tend to fall into two categories. For most computations, accuracies in the order of 8 bits are ample. However, for absolute value calculations, 16 to 18 bits are often required. For example, if a quantization of .001 arc-s is needed to minimize errors in stability calculations, then for a pixel subtending one-half arc-s in an array of 500 pixels, 18 bits is required. It thus appears that 18-bit accuracy would be needed in many cases. This is consistent with the JPL approach which provides for 18 bit input and output data, needed for the precise centroid calculations.

In summary, the total computational load impact is relatively small and can be handled with minimal impact on the hardware. It is necessary to keep track of the A/D rates and the A/D accuracy requirements in order to minimize system cost and complexity.

Section 8

8.0 CONCLUSIONS AND RECOMMENDATIONS

The test results, coupled with recent advances in silicon device processing capabilities, clearly indicate that the CID has great potential as a stellar tracking device in applications with performance requirements such as those for the Space Telescope Fine Guidance Sensor.

Projected performance parameters of a large area CID array designed for star tracking are:

- 20 μm x 20 μm square sensing site; 400 x 400 array
- Noise ≤ 25 carriers/pixel
- Quantum Yield $\geq 40\%$, from 0.4 to 1.0 μm
- Modest cooling requirements, on the order of 0°C
- Low potential cost due to structural simplicity
- Simple peripheral circuitry

Random access and on-chip processing capabilities are potentially useful for further system simplification.

Further effort is indicated to verify the projected CID performance. This includes:

1. Design, fabrication and test of a full 400 x 400 array, including the necessary system definition, low-noise readout electronics, high accuracy data acquisition circuitry, software, etc., to fully evaluate performance in the star tracker mode.
2. Fabrication and test of a breadboard star tracker module using the array developed in 1, above, or as an interim approach, using an existing array design. Using appropriate star image simulation, the breadboard module should be evaluated against previously defined system functional requirements.

PRECEDING PAGE BLANK NOT FILMED 48

Section 9

9.0 REFERENCES

1. Howard, P.E., "Design Study on Charge Injection Devices for Star Tracker Applications," Final Technical Report, Contract No. NAS8-31749, March 1976.
2. Stanton, R.H., Salamon, P.M. and Goss, W.C., "Solid-State Fine Guidance Sensor for the Space Telescope," Phase 1 Final Report.
3. Carnes, J.E. and Kosonocky, "Noise Sources in Charge-Coupled Devices," RCA Revision, 33, June 1977, pp. 327-343.
4. Michon, G.J. et al., "Study of Noise in CID Imagers," Final Report, Contract No. N00173-77-C-0054, November 1978.
5. Yoshikawa, S. and Chikawa, J., "Electrical Effect of Growth Striations in the Silicon Vidicon-Type Camera Tubes," Appl. Phys. Lett., 23, No. 11, December 1, 1973.
6. Dash, W.C. and Newman, R., "Intrinsic Optical Absorption in Single-Crystal Germanium and Silicon at 77°K and 300°K," Phys. Rev., 99, No. 4, August 15, 1955, pp. 1151-55.
7. Stanton, *ibid*, p. 2-2.
8. Stanton, *ibid*, p. 3-8.
9. Stanton, *ibid*, p. 5-13.

PRECEDING PAGE BLANK NOT FILMED SD

Section 10

10.0 APPENDIX

10.1 Calculation of Tracking Accuracy and Stability

This appendix presents the calculation of the radius of stability and accuracy for the limiting cases according to the following specifications:

1. A 3 x 3 pixel matrix is used for centroid calculation.
2. The star image is gaussian with a spread of $\sigma_s =$ one pixel width.
3. The effective aperture area of the lens is $A = 32,000 \text{ cm}^2$.
4. The amount of stellar radiation reaching the lens for a $M_V 0$ star, $I_0 = 3.57 \times 10^6 \text{ photons/cm}^2\text{-s}$.
5. The integration time is $t = .05 \text{ s}$.
6. The combined lens and imager quantum efficiency over the portion of the spectrum of interest is $Q = 0.5 \text{ carriers/photon}$.
7. One pixel width subtends an angle of $.5 \text{ arc-s}$.
8. The level of random temporal noise is 25 carriers.
9. The linearity of response variations are 0.5%.

The centroid calculation is performed on the 3 x 3 pixel matrix shown in Figure A-1.

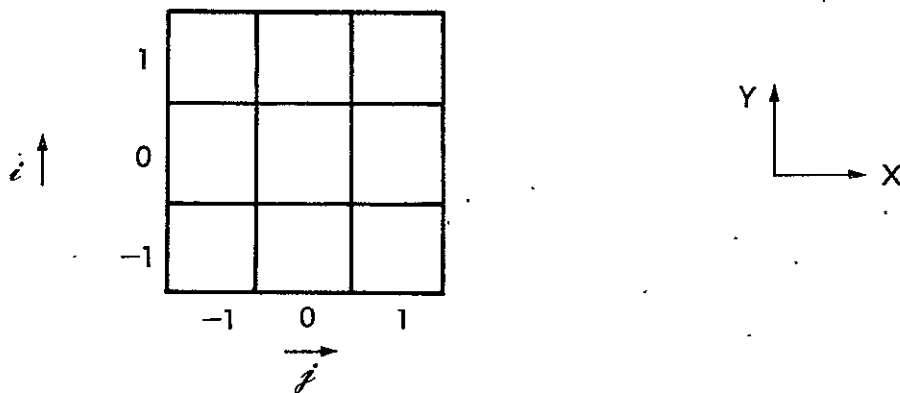


Figure A-1. 3 x 3 Pixel Sub-array

The equations used to calculate the centroid position are:

$$X = \frac{1}{T} \sum_{i=-1}^{+1} \sum_{j=-1}^{+1} j V_{ij} \quad (A1)$$

and

$$Y = \frac{1}{T} \sum_{i=-1}^{+1} \sum_{j=-1}^{+1} i V_{ij} \quad (A2)$$

where V_{ij} is the signal at pixel location (i,j) and

$$T = \sum_{i=-1}^{+1} \sum_{j=-1}^{+1} V_{ij} \quad (A3)$$

is the total signal falling on the 3×3 array.

For large signal-to-noise ratios, the variation in the X direction is

$$dX = \sum_i \sum_j (\partial X / \partial V_{ij}) dV_{ij} \quad (A4)$$

$$\begin{aligned} \text{where } (\partial X / \partial V_{ij}) &= (\partial / \partial V_{ij}) \left[(1/T) \left(\sum_i \sum_j j V_{ij} \right) \right] \\ &= (\partial / \partial V_{ij}) \left[\left(\sum_i \sum_j j V_{ij} \right) / \left(\sum_i \sum_j V_{ij} \right) \right] \\ &= \left(j \sum_i \sum_j V_{ij} - \sum_i \sum_j j V_{ij} \right) / \left(\sum_i \sum_j V_{ij} \right)^2 \\ &= (jT - \sum_i \sum_j j V_{ij}) / T^2 \\ &= \frac{j - X}{T} \end{aligned} \quad (A5)$$

The best case for accuracy and stability is when the star is centered in the matrix and the spread of light is as shown in Figure A-2. The worst case, assuming the 3×3 block can be moved in single-pixel increments, is when the star is in the corner of the center pixel and the spread of light is as shown in Figure A-3.

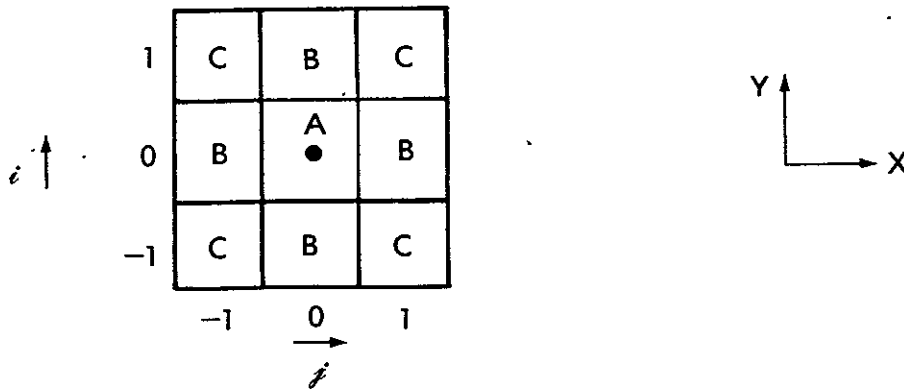


Figure A-2. Light Distribution - Star in Center

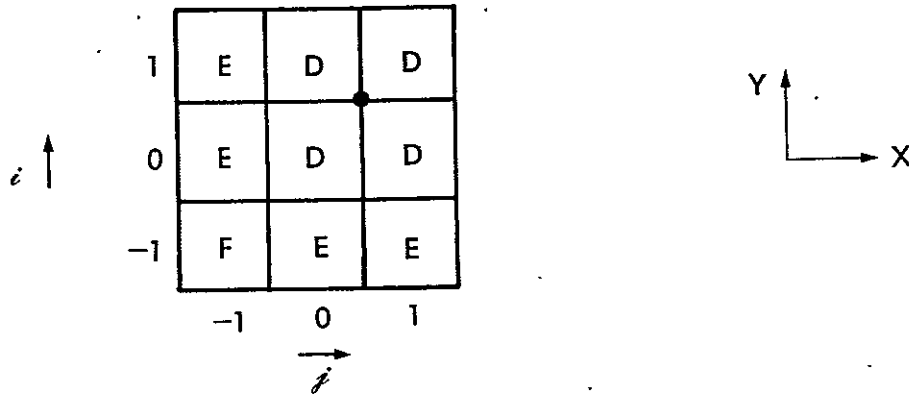


Figure A-3. Light Distribution - Star in Corner

10.1.1 Centered Star

For the case of the centered star, the variance in the X direction is

$$dX^2 = (1/T^2) \sum_i \sum_j (j-X)^2 \sigma_N^2(i,j) \quad (A6)$$

where $\sigma_N^2(i,j)$ is the noise on the (i,j) pixel. In this case

$$X = 0 \text{ and } Y = 0 \quad (A7)$$

The variance in X is

$$\begin{aligned} dX^2 &= (1/T^2) \left\{ 2 \left[(-1)^2 \sigma_N^2(C) + (0)^2 \sigma_N^2(B) + (1)^2 \sigma_N^2(C) \right] \right. \\ &\quad \left. + \left[(-1)^2 \sigma_N^2(B) + (0)^2 \sigma_N^2(A) + (1)^2 \sigma_N^2(B) \right] \right\} \\ &= (1/T^2) \left\{ 4 \sigma_N^2(C) + 2 \sigma_N^2(B) \right\} \end{aligned} \quad (A8)$$

The star's intensity profile is the standard two-dimensional normal distribution,

$$V(X, Y) = (V_0/2\pi\sigma_s) \exp \left[-(X^2 + Y^2)/2 \sigma_s^2 \right] \quad (A9)$$

where V_0 is the total star radiation as measured by the imager,

$$V_0 = (I_0 A Q t)/(2.5)^{M_V} \quad (A10)$$

When the proper values are inserted, this becomes

$$\begin{aligned} V_0 &= (3.57 \times 10^6)(3.20 \times 10^4)(.5)(.05)/(2.5)^{M_V} \\ &= 2.86 \times 10^9/(2.5)^{M_V} \end{aligned} \quad (A11)$$

where M_v , the visual magnitude, has been left as the independant variable.

The star signal which falls on the 3 x 3 array is

$$\begin{aligned}
 T &= \int_{-1.5}^{1.5} \int_{-1.5}^{1.5} V(X,Y) \, dXdY \quad (A12) \\
 &= \int_{-1.5}^{1.5} \int_{-1.5}^{1.5} (V_0/2 \pi \sigma_s) \exp \left[(X^2+Y^2)/2 \sigma_s^2 \right] dXdY \\
 &= (V_0/2\pi\sigma_s) \int_{-1.5}^{1.5} \exp \left[X^2/2 \sigma_s^2 \right] \int_{-1.5}^{1.5} \exp \left[Y^2/2\sigma_s^2 \right] dYdX \\
 &= \left[V_0/(2\pi\sigma_s)^{1/2} \right] \int_{-1.5}^{1.5} \exp \left[X^2/2 \sigma_s^2 \right] \left\{ \left[1/(2\pi)^{1/2} \right] \int_{-1.5}^{1.5} \exp \left[Y^2/2\sigma_s^2 \right] (dY/\sigma_s) \right\} dX
 \end{aligned}$$

or with the substitution $Z = Y/\sigma_s$, this becomes

$$\begin{aligned}
 T &= \left[V_0(2\pi\sigma_s)^{1/2} \right] \int_{-1.5}^{1.5} \exp \left[X^2/2\sigma_s^2 \right] \left\{ \left[1/(2\pi)^{1/2} \right] \int_{-1.5/\sigma_s}^{1.5/\sigma_s} \exp \left[Z^2/2 \right] dZ \right\} dX \quad (A13) \\
 &= \left[V_0/(2\pi\sigma_s)^{1/2} \right] \int_{-1.5}^{1.5} \exp \left[X^2/2\sigma_s^2 \right] \left[\operatorname{erf} \left(\frac{1.5}{\sigma_s} \right) - \operatorname{erf} \left(\frac{-1.5}{\sigma_s} \right) \right] dX
 \end{aligned}$$

The same operation can be used for integrating with respect to X. The result is

$$T = V_0 \left[\operatorname{erf}(1.5/\sigma_s) - \operatorname{erf}(-1.5/\sigma_s) \right]^2 \quad (A14)$$

For $\sigma_s = 1$ pixel width this can be evaluated with the help of Table A-1. The result is

$$\begin{aligned}
 T &= V_0 \left[.433 + .433 \right]^2 \\
 &= .750 V_0 \quad (A15)
 \end{aligned}$$

The variaiance in the x direction is

$$dX^2 = \left[4\sigma_N^2(C) + 2\sigma_N^2(B) \right] / (.750 V_0)^2 \quad (A16)$$

The radius of stability is

$$r_S = (dX^2 + dY^2)^{1/2} \quad (A17)$$

Table A-1
TABLE OF THE ERROR FUNCTION

$$\operatorname{erf} x = \frac{1}{\sqrt{2\pi}} \int_0^x \exp(-y^2/2) dy$$

x	erf x	x	erf x
0.05	0.01994	1.55	0.43943
0.10	0.03983	1.60	0.44520
0.15	0.05962	1.65	0.45053
0.20	0.07926	1.70	0.45543
0.25	0.08971	1.75	0.45994
0.30	0.11791	1.80	0.46407
0.35	0.13683	1.85	0.46784
0.40	0.15542	1.90	0.47128
0.45	0.17364	1.95	0.47441
0.50	0.19146	2.00	0.47725
0.55	0.20884	2.05	0.47982
0.60	0.22575	2.10	0.48214
0.65	0.24215	2.15	0.48422
0.70	0.25804	2.20	0.48610
0.75	0.27337	2.25	0.48778
0.80	0.28814	2.30	0.48928
0.85	0.30234	2.35	0.49061
0.90	0.31594	2.40	0.49180
0.95	0.32894	2.45	0.49286
1.00	0.34134	2.50	0.49379
1.05	0.35314	2.55	0.49461
1.10	0.36433	2.60	0.49534
1.15	0.37493	2.65	0.49597
1.20	0.38493	2.70	0.49653
1.25	0.39435	2.75	0.49702
1.30	0.40320	2.80	0.49744
1.35	0.41149	2.85	0.49781
1.40	0.41924	2.90	0.49813
1.45	0.42647	2.95	0.49841
1.50	0.43319	3.00	0.49865

and since $\overline{dX}^2 = \overline{dY}^2$ at the center,

$$r_S = (2dX^2)^{1/2} \\ = \left[8\sigma_N^2(c) + 4\sigma_N^2(B) \right]^{1/2} / (.750 V_0) \quad (A18)$$

10.1.2 Star in Corner

For the star in the corner of the center pixel, equation (A6) still holds.

$$dX^2 = (1/T^2) \sum_{ij} (j-x)^2 \sigma_n(i,j) \quad (A19)$$

In this case

$$X = .5 \text{ and } Y = .5 \quad (A20)$$

The variance in the X direction is

$$dX^2 = (1/T^2) \left\{ 2 \left[(-1.5)^2 \sigma_N^2(E) + (-.5)^2 \sigma_N^2(D) + (.5)^2 \sigma_N^2(D) \right] \right. \\ \left. + \left[(-1.5)^2 \sigma_N^2(F) + (-.5)^2 \sigma_N^2(E) + (.5)^2 \sigma_N^2(E) \right] \right\} \\ = (1/T^2) \left\{ 2.25 \sigma_N^2(F) + 5 \sigma_N^2(E) + \sigma_N^2(D) \right\} \quad (A21)$$

The star signal which falls on the 3 x 3 array in this case is

$$T = \int_{-2}^1 \int_{-2}^1 V(X,Y) dXdY \\ = V_0 \left[\text{erf}(1/\sigma_S) - \text{erf}(-2/\sigma_S) \right]^2 \quad (A22)$$

With the use of Table A-1, this evaluates to

$$T = V_0 \left[.341 + .477 \right]^2 \\ = 0.669 V_0 \quad (A23)$$

The variance in the X direction is

$$dX^2 = \left[2.25 \sigma_N(F) + 5 \sigma_N(E) + \sigma_N(F) \right] / (.669 V_0)^2 \quad (A24)$$

The radius of stability is

$$r_S = (2dX^2)^{1/2} \quad (A25)$$

$$= \left[4.5 \sigma_N(F) + 10 \sigma_N(E) + 2 \sigma_N(D) \right]^{1/2} / (.699 V_0) \quad (A26)$$

10.1.3 Case A

This case calculates the radius of stability when there is only random, uncorrelated, thermal noise, and assumes that there is no shot noise. Therefore

$$\sigma_N(A) = \sigma_N(B) = \dots = \sigma_N(F) = \sigma_N \quad (A27)$$

The radius of stability for a star that is centered, Case A1, is from equations A18 and A27

$$\begin{aligned} r_S &= (12\sigma_N^2)^{1/2}/(.750V_0) \\ &= 4.62 (\sigma_N/V_0) \end{aligned} \quad (A28)$$

With the noise estimated to be 25 carriers and V_0 as given by equation A11, the radius of stability is

$$\begin{aligned} r_S &= (4.62)(25) (2.5)^{M_V}/2.80 \times 10^9 \\ &= (4.04 \times 10^{-8})(2.5)^{M_V} \text{ pixel widths} \end{aligned} \quad (A29)$$

In arc-s this is

$$r_S = (2.02 \times 10^{-8}) 2.5^{M_V} \text{ arc-s} \quad (A30)$$

This is plotted in Figure 7-2, Curve A1.

The radius of stability for a star centered at the corner of the center pixel, Case A2, is from equations A26 and A27

$$\begin{aligned} r_S &= (16.5\sigma_N^2)^{1/2}/(.669V_0) \\ &= 6.07 (\sigma_N/V_0) \end{aligned} \quad (A31)$$

When the proper values are inserted this gives

$$\begin{aligned} r_S &= (6.07) (25) (2.5)^{M_V}/2.86 \times 10^9 \\ &= (5.31 \times 10^{-8})(2.5)^{M_V} \text{ pixel widths} \end{aligned} \quad (A32)$$

This is equivalent to

$$\begin{aligned} r_S &= (2.65 \times 10^{-8})(2.5)^{M_V} \text{ arc-s} \\ &= 1.32 \text{ times Case A1} \end{aligned} \quad (A33)$$

This is plotted in Figure 7-2, Curve A2

10.1.4 Case B

The other limiting case assumes that there is no thermal noise, only shot noise on the star signal. In order to find the radius of stability for this case, each individual noise level must be calculated from

$$\sigma_N(i,j) = [V(i,j)]^{1/2} \quad (A34)$$

When the star is centered, Case B1, V(B) and V(C) must be calculated. They are

$$\begin{aligned} V(B) &= \int_{-.5}^{.5} \int_{.5}^{1.5} V(X,Y) dXdY \\ &= V_0 [\text{erf}(.5\sigma_s) - \text{erf}(-.5\sigma_s)] [\text{erf}(1.5/\sigma_s) - \text{erf}(.5/\sigma_s)] \\ &= V_0 [.191 + .191] [.433 - .191] \\ &= .0924 V_0 \end{aligned} \quad (A35)$$

and

$$\begin{aligned} V(C) &= \int_{.5}^{1.5} \int_{.5}^{1.5} V(X,Y) dXdY \\ &= V_0 [\text{erf}(1.5/\sigma_s) - \text{erf}(.5/\sigma_s)]^2 \\ &= V_0 [.433 - .191]^2 \\ &= .0586 V_0 \end{aligned} \quad (A36)$$

The radius of stability is from equations A18, A34, A35, and A36

$$\begin{aligned} r_s &= [8 (.0586V_0) + 4 (.0924V_0)]^{1/2} / (.750 V_0) \\ &= 1.22/(V_0)^{1/2} \\ &= [(1.22)(2.5)^{M_V/2}] / (2.86 \times 10^9)^{1/2} \\ &= (2.28 \times 10^{-5})(2.5)^{M_V/2} \text{ pixel widths} \\ &= (1.14 \times 10^{-5})(2.5)^{M_V/2} \text{ arc-s} \end{aligned} \quad (A37)$$

This result is plotted in Figure.7-2, Curve B1.

When the center of the star falls in the corner of the 3 x 3 array, Case B2, V(D), V(E), and V(F) must be calculated. They are

$$V(D) = \int_0^1 \int_0^1 V(XY) dXdY$$

$$\begin{aligned}
 &= V_0 \left[\operatorname{erf}(1/\sigma_S) \right]^2 \\
 &= V_0 \left[.341 \right]^2 \\
 &= .116 V_0
 \end{aligned} \tag{A38}$$

and

$$\begin{aligned}
 V(E) &= \int_0^1 \int_1^2 V(XY) dXdY \\
 &= V_0 \left[\operatorname{erf}(1/\sigma_S) \right] \left[\operatorname{erf}(2/\sigma_S) - \operatorname{erf}(1/\sigma_S) \right] \\
 &= V_0 \left[.341 \right] \left[.477 - .341 \right] \\
 &= .0464 V_0
 \end{aligned} \tag{A39}$$

and

$$\begin{aligned}
 V(F) &= \int_1^2 \int_1^2 V(XY) dXdY \\
 &= V_0 \left[\operatorname{erf}(2/\sigma_S) - \operatorname{erf}(1/\sigma_S) \right]^2 \\
 &= V_0 \left[.477 - .341 \right]^2 \\
 &= .0185 V_0
 \end{aligned} \tag{A40}$$

The radius of stability is, from equations A26, A34, A38, A39, and A40

$$\begin{aligned}
 r_S &= \left[4.5(.0185 V_0) + 10(.0464 V_0) + 2 (.116 V_0) \right]^{1/2} / (.699 V_0) \\
 &= 1.32 / (V_0)^{1/2} \\
 &= \left[(1.32)(2.5)^{M_V/2} \right] / (2.86 \times 10^9)^{1/2} \\
 &= (2.47 \times 10^{-5})(2.5)^{M_V/2} \text{ pixel widths} \\
 &= (1.23 \times 10^{-5})(2.5)^{M_V/2} \text{ arc-s} \\
 &= 1.08 \text{ times the result of Case B1}
 \end{aligned} \tag{A41}$$

This result is plotted in Figure 7-2, Curve B2.

10.1.5. Case C

For this case the radius of accuracy is calculated. In addition to the random noise results of Case A and Case B, there will be a fixed pattern noise due to (1) random effects such as threshold variations and (2) linearity of

response variations. The double read method is expected to cancel the random (but positionally stable) fixed pattern noise to the extent where is insignificant. The linearity of response variations are estimated to be .5% or

$$\alpha = .005 \quad (A42)$$

and so the noise is

$$\sigma_n(XY) = \alpha \hat{V}(XY) \quad (A43)$$

When the star is centered, Case C1, the radius of accuracy is, from equation A18,

$$r_A = \left[8\sigma_n^2(C) + 4\sigma_n^2(B) \right]^{1/2} / (.750 V_o) \quad (A44)$$

With the use of equation (A43) this becomes

$$r_A = \left[8\alpha^2 \overline{V(C)^2} + 4\alpha^2 \overline{V(B)^2} \right]^{1/2} / (.750 V_o) \quad (A45)$$

and from equations A35 and A36, this becomes

$$\begin{aligned} r_A &= \left[8\alpha^2 (.0586 V_o)^2 + 4\alpha^2 (.0924 V_o)^2 \right]^{1/2} / (.750 V_o) \\ &= \alpha [.331] \\ &= .005 [.331] \\ &= .00166 \text{ pixel widths} \\ &= .000828 \text{ arc-s} \end{aligned} \quad (A46)$$

This result is plotted in Figure 7-2, Curve C1

When the star is centered in the corner of the center pixel, the radius of accuracy is, from equation A26,

$$r_A = \left[4.5\sigma_n^2(F) + 10\sigma_n^2(E) + 2\sigma_n^2(D) \right] / (.669 V_o) \quad (A47)$$

With the use of equation (A43) this is

$$r_A = \left[4.5\alpha^2 \overline{V(F)^2} + 10\alpha^2 \overline{V(E)^2} + 2\alpha^2 \overline{V(D)^2} \right] / (.669 V_o) \quad (A48)$$

When this result is combined with equations A38, A39, and A40, it gives

$$r_A = \left[4.5\alpha^2 (.0185 V_o)^2 + 10\alpha^2 (.0464 V_o)^2 + 2\alpha^2 (.116 V_o)^2 \right]^{1/2} / (.669 V_o)$$

$$\begin{aligned} &= \alpha (.335) \\ &= (.005)(.335) \\ &= .00167 \text{ pixel widths} \\ &= .000837 \text{ sec} \\ &= 1.01 \text{ times the result of Case C1} \end{aligned} \tag{A49}$$

This result is plotted in Figure 7-2, Curve C2.

1. Report No NAS8-32801		2. Government Accession No.		3. Recipient's Catalog No	
4. Title and Subtitle DESIGN, FABRICATION, AND DELIVERY OF A CHARGE INJECTION DEVICE AS A STELLAR TRACKING DEVICE				5. Report Date April 1979	
				6. Performing Organization Code	
7. Author(s) H.K. Burke, G.J. Michon, H.W. Tomlinson, T.L. Vogelsong,* A. Grafinger, R. Wilson**				8. Performing Organization Report No SRD-78-171	
				10. Work Unit No	
9. Performing Organization Name and Address General Electric Company *Corporate Research and Development **Aerospace Business Group Signal Electronics Lab Re-Entry & Environmental Systems Schenectady, NY 12305 Research & Engineering Dept. Philadelphia, PA 19101				11. Contract or Grant No	
				13. Type of Report and Period Covered Final Technical Report 28 November 77 - 28 November 78	
12. Sponsoring Agency Name and Address National Aeronautics and Space Administration George C. Marshall Space Center Huntsville, Alabama 35812				14. Sponsoring Agency Code	
15. Supplementary Notes Project Manager, C.S. Jones Marshall Space Flight Center Huntsville, Alabama 35812					
16. Abstract Six 128 x 128 CID imagers fabricated on bulk silicon and with thin polysilicon upper-level electrodes were tested in a star tracking mode. Noise and spectral response were measured as a function of temperature over the range of +25°C to -40°C. Noise at 0°C and below was less than 40 rms carriers/pixel for all devices at an effective noise bandwidth of 150 Hz. Quantum yield for all devices averaged 40% from 0.4 to 1.0 μm with no measurable temperature dependence. Extrapolating from these performance parameters to those of a large (400 x 400) array and accounting for design and processing improvements, indicates that the larger array would show a further improvement in noise performance -- on the order of 25 carriers. A preliminary evaluation of the projected performance of the 400 x 400 array and a representative set of star sensor requirements (Fine Guidance Sensor for the Space Telescope) indicates that the CID has excellent potential as a stellar tracking device. Further theoretical and experimental evaluation of CID performance in this application is recommended.					
17. Key Words (Suggested by Author(s)) CID imaging, star tracking, solid-state imaging, low noise imaging, stellar tracking sensor				18. Distribution Statement Unclassified - Unlimited	
19. Security Classif. (of this report) Unclassified		20. Security Classif. (of this page) Unclassified		21. No. of Pages 63	22. Price*

* For sale by the National Technical Information Service, Springfield, Virginia 22161